POLITECNICO DI TORINO

College of Chemical and Materials Engineering

**Master of Science Course**
**in Materials Engineering for Industry 4.0**

Master of Science Thesis

# Fabrication of a Coriolis effect-based MEMS sensor for metrology applications


**Tutors**
Prof. Giancarlo Cicero, Politecnico di Torino
Dr. Diego Pugliese, INRiM
Dr. Giuseppe Cavuoto, INRiM
Dr. Simone Luigi Marasso, CNR

**Candidate**
Vincenzo Della Donna

July 2026

# *Abstract*

This work presents the modeling, microfabrication, and experimental characterization of a micro-Coriolis mass flow sensor fabricated entirely from SU-8 100. The device utilizes the Coriolis effect to obtain a direct measurement of mass flow rate that is independent of the fluid's physical properties, such as density and viscosity. The choice of the SU-8 epoxy photoresist was driven by its biocompatibility, as well as its mechanical properties, such as mechanical and thermal stability which make it ideal for integration into micro electro-mechanical systems (MEMS) intended for biomedical and industrial applications.

The fabrication process has evolved from the use of traditional ultraviolet (UV) photolithography to direct write lithography (DWL), in order to ensure rapid and flexible prototyping for MEMS architectures. The device structure was fabricated using a multi-layer process involving the separate fabrication of microfluidic bases and covers through optimized steps of spin coating, soft bake, laser exposure, and post-exposure bake (PEB).

A critical phase of the research involved the hermetic integration of the two components (bases and covers) through hot embossing bonding, which ensured the structural stability and watertight seal of the microchannel, as validated by microfluidic leak tests.

The device was characterized using piezoelectric actuation, integrated with a laser Doppler vibrometer (LDV) detection system, to obtain the frequency response of various fluids of known density. The results validated the instrument's operation, experimentally confirming the effectiveness of the architecture and the transduction principle adopted.

Looking ahead, the piezoelectric actuation will be implemented directly on the sensor. A readout system will also be integrated to measure the torsional vibration of the microchannel caused by the Coriolis force, which will enable accurate measurement of the mass flow rate. Concurrently, grayscale lithography will be optimized for the fabrication of complex three-dimensional (3D) topographies.

# Nomenclature

| Quantity | Symbol | Unit |
|---|---|---|
| **Geometric quantities** | | |
| Length vector | $\vec{L}$ | m |
| Internal geometric volume | $V_{ch}$ | $m^3$ |
| Geometric overlap area | $A$ | $m^2$ |
| Gap distance | $d_0$ | m |
| Displacement | $\Delta x$ | m |
| **Temporal and frequency quantities** | | |
| Time | $t$ | s |
| Absolute time delay | $\tau$ | s |
| Phase shift | $\Delta\theta$ | rad |
| Natural resonance frequency | $f_0$ | Hz |
| Resonance frequency shift | $\Delta f$ | Hz |
| Angular velocity vector | $\vec{\omega}$ | rad/s |
| Drive mode angular frequency | $\omega drive$ | rad/s |
| **Mechanics and dynamics** | | |
| Mass flow rate | $\Phi_m$ | kg/s |
| Volumetric flow rate | $Q$ | $m^3/s$ |
| Coriolis force vector | $\vec{F}_c$ | N |
| Lorentz force vector | $\vec{F}_L$ | N |
| Mass of the empty channel | $m_{ch}$ | kg |

| | | |
|---|---|---|
| Mass density | $\rho$ | kg/m$^3$ |
| Drive mode elastic constant | $k_D$ | N·m/rad |
| Sense mode torsional stiffness | $Ksense$ | N·m/rad |
| Angular deflection (drive/sense) | $\phi drive, \phi sense$ | rad |
| **Electricity and magnetism** | | |
| Alternating current intensity | $I$ | A |
| Magnetic flux density vector | $\vec{B}$ | T |
| Capacitance variation | $\Delta C$ | F |
| Permittivity of free space | $\varepsilon_0$ | F/m |
| Relative permittivity | $\varepsilon_r$ | — |
| **Material properties** | | |
| Young's modulus | $E$ | Pa |
| Poisson's ratio | $v$ | — |
| Glass transition temperature | $T_g$ | °C |
| **Calibration and statistical parameters** | | |
| Residuals | $res_i$ | kg/ m$^3$ |
| Root mean square error | $RMSE$ | % |
| Relative uncertainty | $u_{r\,\%}$ | |
| Combined standard uncertainty | $u_c$ | % |
| Expanded percentage uncertainty | $U_{\rho}$ % | % |
| Coverage factor | $k$ | — |

*Il traguardo non è in queste pagine, ma nella persona che è stata necessaria per scriverle. Se un giorno il dubbio oscurerà il suo coraggio, che sia questo cammino a ricordargli quanto lontano può arrivare.*

# INDEX

# 1 Introduction

The evolution of miniaturized total analysis systems (μ-TAS) and lab-on-a-chip (LOC) platforms has imposed increasingly stringent accuracy requirements for handling fluid flow rates below 1 g/h in applications such as biomedical diagnostics and drug delivery [1, 2, 3]. At these scales, however, conventional measurement techniques are highly sensitive to the thermophysical and rheological variations of biological fluids [2, 4]. To overcome this limitation, micro-Coriolis mass flow sensor (MCMFS) technology has emerged as one of the most promising solutions. These devices operate on the principle of conservation of angular momentum within a vibrating microchannel. By exploiting the resonant excitation of a suspended structure (drive mode) [1, 2, 5], they generate Coriolis forces directly proportional to the mass flow rate of the fluid passing through the channel, enabling direct flow measurement independent of the fluid's density and viscosity [1, 5, 6]. Acting orthogonally to both the fluid velocity vector and the axis of rotation, these forces induce a secondary mechanical torque that excites an asymmetric out-of-plane vibration mode (sense mode). Furthermore, under steady-state flow conditions, real-time monitoring of the resonance frequency shift caused by the additional mass of the liquid allows the same device to simultaneously operate as a high-precision densimeter.

Although the current state of the art provides well-established solutions based on silicon and silicon nitride, the associated bulk micromachining processes entail high manufacturing costs and significant process complexity, limiting their applicability in disposable or low-cost devices [1, 6, 7]. This thesis addresses this limitation by investigating the development of a micro-Coriolis sensor fabricated entirely from SU-8 100, an epoxy-based photoresist capable of producing thick, chemically inert polymer structures [3, 8]. However, transferring a resonant sensing structure to a polymeric material introduces substantial engineering challenges due to the low elastic modulus and high intrinsic damping of SU-8 [1].

The focus of this project was the complete redesign and optimization of the microfluidic system through a comprehensive revision of the fabrication process and targeted modifications to the geometry of the individual layers. From a microfabrication perspective, the work concentrated on the transition to maskless laser direct writing (LDW) technology using the Heidelberg Instruments DWL 66+ system [9]. This approach enabled rapid and flexible prototyping of complex micro electro-mechanical systems

(MEMS) structures. In parallel, the critical bonding parameters were identified using the EVG 510 bonding press [10], with all experimental activities carried out at the Piemonte Quantum Enabling Technology (PiQuET) facility within the National Institute of Metrological Research (INRiM). The primary challenge consisted of optimizing the process parameters and defining a suitable geometry capable of ensuring hermetic sealing of the suspended microchannels under high-pressure conditions while preventing delamination.

In addition to consolidating the manufacturing process and evaluating its reproducibility and scalability for the simultaneous production of multiple devices, the study presents a conceptual model of the integrated actuation system in preparation for the future implementation of the complete measurement device.

## 1.1 Comparative analysis of MEMS Coriolis technologies

The first MCMFSs were developed using bulk silicon micromachining processes. Enoksson et al. [11] fabricated resonant tubes from monocrystalline silicon using anisotropic etching and anodic bonding on glass substrates, combining electrostatic actuation and optical detection systems [6, 11].

A significant technological advancement was subsequently introduced by surface channel technology (SCT), which enables the fabrication of suspended microchannels in silicon nitride with extremely thin walls, down to approximately 1.2 μm [2, 12]. The significant reduction in the mass of the resonator relative to that of the contained fluid has made it possible to substantially increase the device's sensitivity, extending the detection limit to flow rates in the order of milligrams and micrograms per hour. The most recent developments have also led to the integration of dedicated complementary metal-oxide-semiconductor (CMOS) circuits for signal control and digital conversion, enabling zero-point stability of less than ± 0.31 mg/h [4].

Despite the high performance achieved, the complexity of semiconductor-based manufacturing processes and the associated production costs have stimulated research into alternative solutions. In this context, the use of structural polymer materials, particularly the SU-8 epoxy photoresist, represents a promising opportunity for the development of low-cost micro-Coriolis sensors compatible with disposable microfluidic applications.

### 1.1.1 Silicon micromachining and bonding techniques

The first Coriolis MEMS sensors described in the literature took advantage of the high mechanical properties of bulk monocrystalline silicon, a material that ensures elastic behavior and high fatigue resistance under high frequency oscillation cycles. In the context of this technological evolution, one of the most well-established configurations involves the fabrication of silicon microtubes integrated onto metallized glass substrates, an architecture that has been extensively documented in the early pioneering work by Enoksson et al. [11] and in subsequent commercial developments by Smith et al. [6] for industrial applications (Figure 1.1).

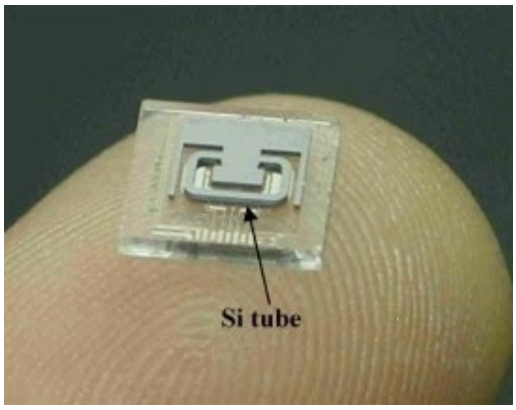


*Figure 1.1 Architecture of the microfluidic chip and resonant microtube [6].*

The fabrication process typically begins with plasma etching of the internal microchannel into a bulk silicon wafer, using anisotropic dry etching techniques such as reactive ion etching (RIE) or deep reactive ion etching (DRIE). The wafer is then bonded to a second silicon substrate through fusion bonding to hermetically seal the channel. This bonding process involves high temperature thermal treatments that promote the formation of stable covalent bonds. Subsequently, the external geometry of the tube and the resonant microstructure are defined by photolithography followed by an additional DRIE step performed from the backside of the wafer, enabling precise control over the thickness and stiffness of the structural walls. Finally, the silicon structure is suspended and integrated onto a Pyrex glass substrate through anodic bonding (Figure 1.2). This process creates a permanent bond through ion migration induced by high voltages and moderate temperatures, allowing the tube to interface with metal electrodes previously deposited on the glass substrate for capacitive sensing and device actuation [6, 11].

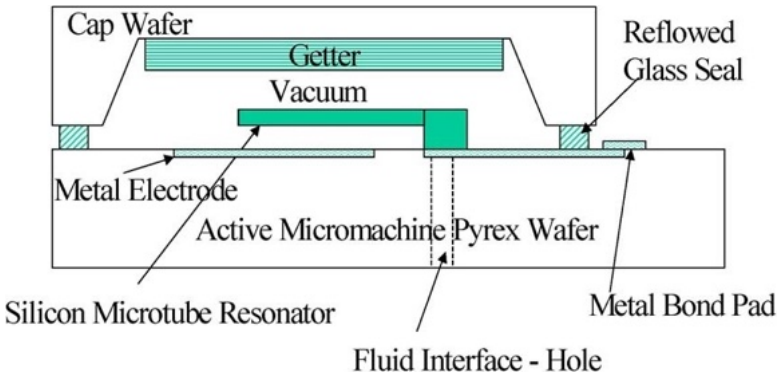


*Figure 1.2 Side cross-sectional schematic of the MEMS device [6].*

The main advantage of this architecture lies in its robustness, which allows it to operate at high static pressures exceeding 100 bar [6]. However, its primary metrological limitation arises from the high structural mass of the bulk silicon tube compared with the mass of the fluid flowing through the microchannel. This inertial imbalance reduces the influence of the extremely small Coriolis forces generated at low flow rates, thereby significantly compromising the sensitivity of the microresonator. Furthermore, this technology presents substantial challenges related to packaging and fluidic interfacing. The connection between the external macroscopic tubing and the microscopic inlets of the silicon chip introduces localized mechanical stresses and thermal drifts resulting from the mismatch in the coefficients of thermal expansion (CTE) of silicon, Pyrex, and the fluidic fittings. These parasitic couplings are transmitted to the vibrating structure, causing shifts in its resonance frequency and degrading long-term zero stability. In addition, the complexity of the multilayer sealing process reduces manufacturing yield and increases the cost per device, limiting its suitability for cost sensitive biomedical applications.

### 1.1.2 Surface channel technology

To overcome the metrological and structural limitations associated with the substantial inertia of silicon-based flow tubes, research efforts have led to the development of SCT, which was primarily developed and optimized at the University of Twente [2]. This architecture was specifically conceived to maximize sensor sensitivity at ultra-low flow rates by drastically reducing the mass of the vibrating structure relative to the mass of the fluid flowing through the channel.

The fabrication process is based on the low-pressure chemical vapor deposition (LPCVD) of a nanometer scale layer of silicon rich nitride (SiRN). Subsequently, a sacrificial chromium mask is patterned through a first photolithographic step, exposing a series of suitably designed and distributed micro-openings or longitudinal slots along the profile of the future channel. The process then proceeds with an isotropic etching step, during which the underlying silicon bulk is chemically removed through the openings in the nitride layer using a sulfur hexafluoride ($SF_6$)-based plasma etch. This isotropic process creates a cavity beneath the surface ceramic layer, thereby defining the geometry of the microchannel. A second and significantly thicker SiRN deposition serves a dual purpose: it hermetically seals the evacuation openings and determines the final thickness of the tube walls, which are typically as thin as 1.2 μm for an internal channel diameter of approximately 40 μm [2, 12]. The final fabrication stage consists of releasing the structure by selectively removing the silicon surrounding and underlying the channel, either through anisotropic wet etching in a potassium hydroxide (KOH) solution or by means of an additional backside anisotropic plasma etching process. This step leaves the SiRN tube, typically configured in a U-shaped or ring-shaped geometry, fully suspended and free to vibrate (Figure 1.3).

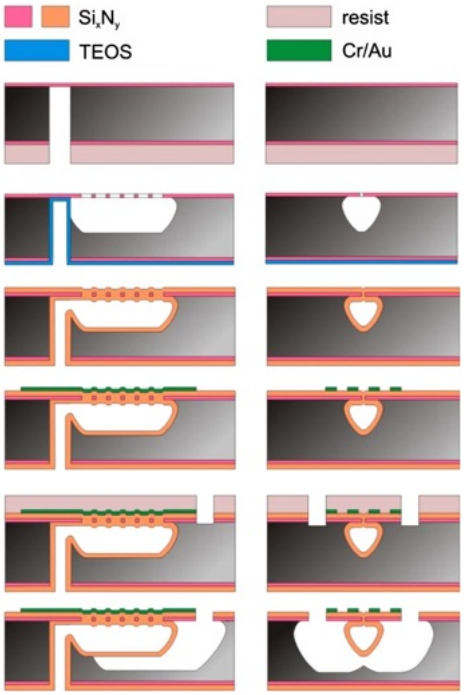


*Figure 1.3 Fabrication process flow. Left: longitudinal cross-sectional view of the microtube. Right: cross-sectional view of the sensing tube [2].*

The actuation of micro-Coriolis sensors is traditionally achieved through the Lorentz force, generated by passing an alternating electric current, $i_a(t)$, through a conductor immersed in an external magnetic field, $B$, as shown in Figure 1.4.

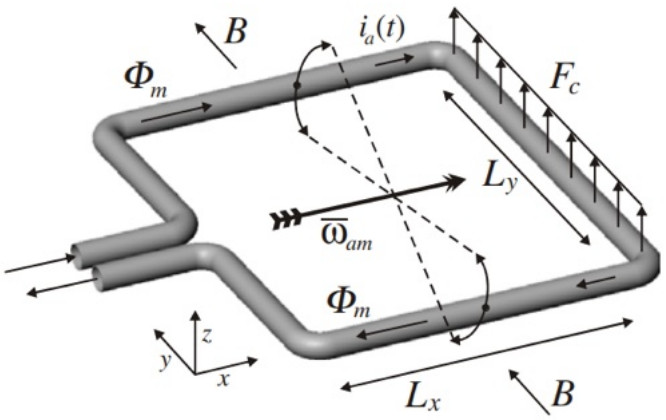


*Figure 1.4 Schematic representation of Lorentz force actuation used to drive the resonant structure [2].*

From a metrological perspective, SCT offers particularly high performance in the measurement of flow rates below 1.2 g/h, owing to the use of ultra-thin walled channels that maximize the fluid to structural mass ratio, thereby generating measurable phase shift signals even at extremely low flow rates. The integration of comb-shaped capacitive electrodes (Figure 1.5 b,c) reduces squeeze film damping, enabling the device to operate at atmospheric pressure with high quality factors without the need for complex vacuum packaging solutions [12]. Furthermore, the coupling with CMOS-based readout circuits operating as oscillation to digital converters (ODCs) with differential modulation suppresses flicker noise, ensuring a zero stability higher than ± 0.31 mg/h [4].

To overcome the thermomechanical limitations associated with Joule heating, which alters the fluid temperature and induces parasitic drifts in the Young's modulus of the structural nitride layer, Zeng et al. [12] introduced a piezoelectric actuation scheme by integrating a thin film of lead zirconate titanate (PZT) onto the SiRN shell (Figure 1.5 a,d). This high impedance actuation system operates with virtually negligible power dissipation, thereby eliminating self-heating effects and significantly improving the thermal stability of the sensor response.

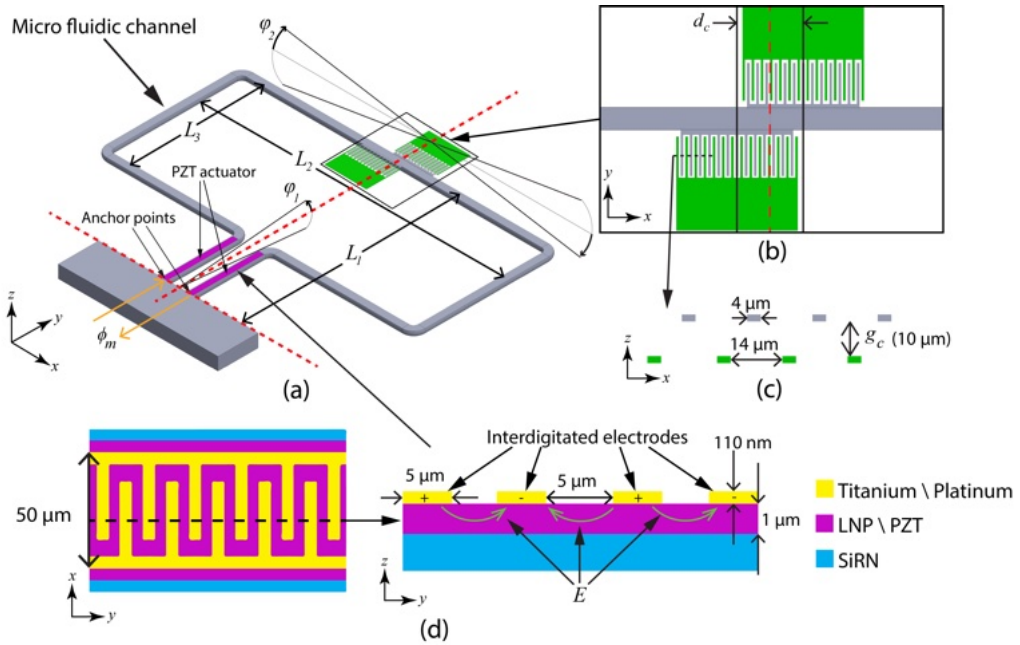


*Figure 1.5 Schematic representation of the microfluidic Coriolis mass flow sensor: (a) Suspended channel actuated by PZT piezoelectric actuators, vibrating in swing and twist modes. (b, c) Comb-shaped capacitive readout system for detecting channel motion. (d) Structure of the piezoelectric actuator with interdigitated platinum electrodes [13].*

However, SCT suffers from severe structural and economic drawbacks. The SiRN-based tube can withstand pressures of only a few bars, rendering it vulnerable to catastrophic cracking under water-hammer conditions. In addition, the numerous high temperature LPCVD deposition steps significantly increase fabrication complexity and capital costs, ultimately confining the technology to specialized niche applications.

### 1.1.3 SU-8 microfabrication

A particularly innovative approach in the field of resonant flow meters is represented by sensors fabricated entirely from SU-8, a permanently cross-linked negative epoxy-based photoresist. This technology emerged from the need to significantly reduce manufacturing costs by eliminating the reliance on highly complex high temperature and high vacuum processes, such as LPCVD deposition and bulk silicon fusion bonding. At the same time, it provides the intrinsic chemical biocompatibility required for the integration of the device into disposable biomedical and clinical applications [1].

The fabrication of SU-8 microfluidic devices is based on a sequential multilayer approach that combines photolithography, spin coating deposition, and thermomechanical bonding processes. The fabrication sequence begins with the definition of the lower and lateral fluidic cavity geometry, where successive SU-8 layers are deposited by spin coating onto temporary silicon or glass carrier substrates. Each layer undergoes a soft bake step to ensure controlled solvent evaporation, followed by selective ultraviolet (UV) exposure and a post-exposure bake (PEB), which is required to activate the cross-linking of the photosensitive material. Repetition of these steps enables the fabrication of high aspect ratio three-dimensional (3D) structures and allows precise definition of both the microchannel geometry and its sidewalls (Figure 1.6) [1].

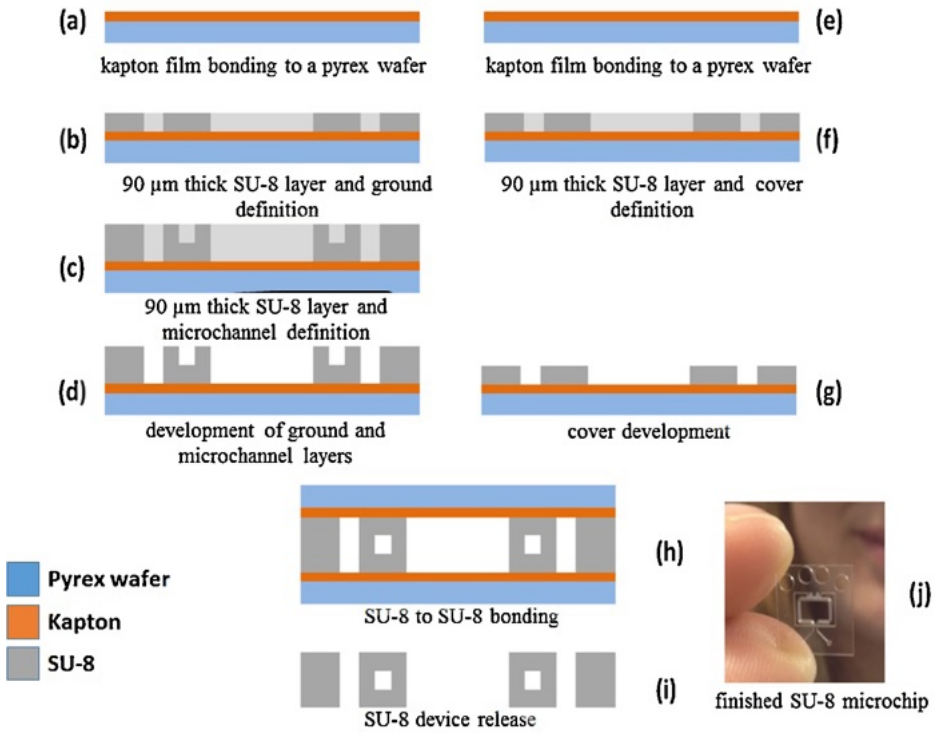


*Figure 1.6 Schematic illustration of the SU-8 microchip fabrication process [1].*

Once the fluidic cavity has been defined, the device is sealed by bonding an SU-8-based layer to the substrate containing the microchannel (Figure 1.6). This SU-8 to SU-8 bonding step represents one of the most critical stages of the entire fabrication process, as it must simultaneously ensure hermetic sealing of the channel while preserving its geometrical integrity. To promote polymer chain interdiffusion and the subsequent irreversible molecular cross-linking at the interfacing surfaces (without inducing parasitic occlusions or structural collapse of the hollow channel) the process requires the simultaneous and carefully controlled application of mechanical pressure, typically ranging from (1 to 3) bar, and temperature within the range of (90 and 170) °C [1].

From a fluid dynamic and metrological perspective, the transition to an SU-8-based structure introduces significant design trade-offs. The low Young's modulus of the polymer (approximately 4.4 GPa, compared with 210 GPa for silicon nitride) and the intrinsic viscoelastic dissipation mechanisms reduce the quality factor of the resonator operating in air. Nevertheless, this reduced structural stiffness is compensated through the adoption of larger channel dimensions, typically featuring a cross-sectional area of

$100 \times 100$ μm$^2$ and structural walls approximately 100 μm thick [1]. This increase in scale provides a key fluid dynamic advantage over SCT, as it enables the handling of relatively high flow rates (up to several hundreds of mg/min) while maintaining hydraulic pressure losses below 1 bar. As a result, the bulky and complex flow bypass architectures commonly employed in industrial applications are no longer required [13], substantially simplifying the overall fluidic layout.

Furthermore, in the present thesis work, the dimensions of the microchannel were further reduced, achieving an internal cross-section of approximately $90 \times 50$ μm$^2$. This geometrical optimization increased the fluid to structural mass ratio, thereby enhancing the sensitivity of the sensor. Such miniaturization enables operation at lower flow rates, improving measurement resolution and extending the applicability of the device to ultra-low flow applications.

### 1.1.4 Comparative analysis and design rationale

The adoption of the SU-8 epoxy-based photoresist as a structural material for the fabrication of Coriolis mass flow sensors (CMFSs) has been widely reported as a viable alternative to conventional ceramic materials, such as single crystalline silicon and silicon nitride.

From a manufacturing perspective, SU-8 enables a substantial reduction in fabrication costs by relying on standard UV photolithography processes, thereby avoiding highly complex and expensive techniques such as LPCVD deposition and bulk silicon micromachining. The scalability afforded by wafer level processing, combined with the intrinsic biocompatibility of the material, makes this technology particularly attractive for the production of disposable devices intended for biomedical diagnostic applications.

From a technological standpoint, the polymer enables the fabrication of high aspect ratio structures with nearly vertical channel sidewalls, providing greater design flexibility than that offered by the geometric constraints associated with anisotropic silicon etching. Although SU-8 exhibits lower mechanical performance than ceramic materials and is characterized by more pronounced intrinsic damping mechanisms, the literature demonstrates that these limitations can be effectively mitigated through careful geometric optimization and the implementation of efficient actuation schemes, such as Lorentz force actuation [1]. These design strategies ensure accurate flow rate measurements while maintaining sufficient structural robustness for the intended operating pressures.

In summary, SU-8 represents an effective technological compromise between fabrication simplicity, low manufacturing costs, and application versatility.

To provide a concise overview of the differences among the available manufacturing approaches, Table 1.1 presents a direct comparison of the various technologies, highlighting their principal advantages and disadvantages with respect to both metrological and economic constraints.

*Table 1.1 Comparative analysis of the main manufacturing technologies for MCMFSs.*

| ***Technology*** | ***Advantages*** | ***Disadvantages and limitations*** | ***References*** |
|---|---|---|---|
| ***Bulk silicon and Pyrex*** | Excellent elastic properties, absence of mechanical fatigue, high resistance to static pressures exceeding 100 bar | High structural mass, low sensitivity at low flow rates, concentrated mechanical stresses, and thermal drifts | [6, 11] |
| ***Surface channel technology (SCT) in silicon nitride*** | Ultra-thin structural mass, high sensitivity for flow rates below 1.2 g/h, compatibility with PZT piezoelectric films | High mechanical fragility under water-hammer conditions, complex and costly fabrication workflows (LPCVD), limited operating pressure range | [2, 12] |
| ***SU-8 epoxy polymer*** | Fabrication cost reduction, standard and fast photolithography processes, high aspect ratio (>15), optical transparency (>360 nm), and disposable biocompatibility | Low Young's modulus (4.4 GPa), high intrinsic viscoelastic damping, high sensitivity to thermocompression bonding parameters | [1, 13] |

## 1.2 Operating principle

The operation of the MCMFS is based on the dynamic interaction between a moving fluid and a vibrating mechanical structure. The core of the sensor consists of a suspended microchannel, typically featuring a rectangular, loop-shaped, or U-shaped geometry, which is driven into forced vibration at a specific natural resonance frequency. When a fluid flows through the channel at a given mass flow rate, each infinitesimal fluid element undergoes a change in its angular velocity due to the rotational motion imposed by the vibrating structure. This gyroscopic interaction generates a Coriolis force, $\overrightarrow{F_c}$, distributed along the length of the channel, as defined in Equation 1.1:

$$\overrightarrow{F_c} = -2\Phi_m(\vec{\omega} \times \vec{L}) \tag{1.1}$$

where $\Phi_m$ [kg/s] represents the fluid mass flow rate, $\vec{\omega}$ [rad/s] denotes the angular velocity vector of the structural oscillation, and $\vec{L}$ [m] defines the vector associated with the geometric length of the suspended channel segment through which the flow passes. The resulting force acts in a direction strictly orthogonal both to the fluid linear velocity vector and to the rotation axis of the vibrating structure and is inherently independent of the physical properties or the type of fluid flowing within the channel.

The resulting force distribution gives rise to an out of plane vibrational mode, orthogonal to the primary torsional mode. The amplitude of this secondary response constitutes the sensing signal of the microsensor and is linearly proportional to the fluid mass flow rate, enabling a direct measurement that is independent of the rheological and thermal properties of the sample under investigation.

The dynamic behavior of the microsensor can be appropriately described using a lumped parameter model that accounts for the energetic interaction between two main resonance modes, namely the drive mode and the sense mode. In the actuation mode, or drive mode, the structure is externally excited to oscillate in a primary torsional mode about a central symmetric axis at a specific angular velocity, whereas in the sensing mode, or sense mode, the Coriolis force induced by the flow generates a secondary mechanical moment that excites an out of plane vibration mode, known as the swing or flapping mode (Figure 1.7).

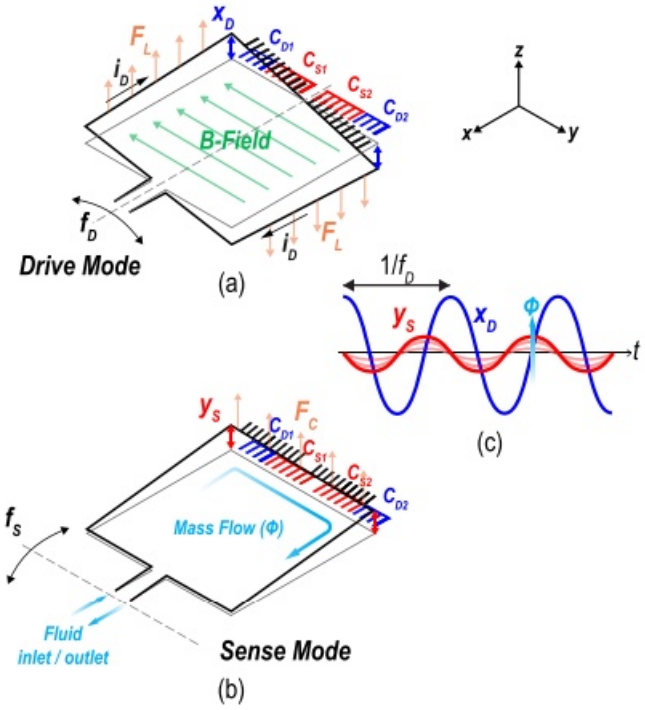


*Figure 1.7 Operating principle of the MEMS Coriolis mass flow sensor with Lorentz force actuation: (a) resonance oscillation in drive mode; (b) excitation of the sense mode induced by the Coriolis force; (c) time domain displacement of the drive (xD) and sense (yS) coordinates [4].*

It is important to highlight a clarification regarding the configuration of the device resonance modes investigated in this work with respect to the models reported in the literature (Figure 1.7). Compared to classical architectures, such as the pioneering device proposed by Monge et al. [1], the system developed in this study features a mirror inverted dynamic transduction chain and resonance mode configuration. In conventional systems, Lorentz force-based actuation excites a torsional mode as the primary drive mode, while the Coriolis force induces an out of plane flexural oscillation as the sense mode response. In contrast, the proposed layout employs piezoelectric actuators to excite a swing mode oscillation as the drive mode; the resulting Coriolis forces then activate a secondary asymmetric torsional mode as the sense mode response.

From a physical and dynamic standpoint, the amplitude of the vibration associated with the sense mode is directly proportional to the mass flow rate of the fluid. The ratio between the angular amplitude of the sense mode and that of the drive mode can be

expressed as a function of the geometric and mechanical parameters of the system as follows (Equation 1.2):

$$\frac{\phi sense}{\phi drive} \propto \frac{\Phi_m \cdot \omega drive}{Ksense} \tag{2.2}$$

In this expression, the dimensionless term on the left-hand side defines the ratio between the angular deflection amplitude of the sense mode, denoted as $\phi sense$ [rad], and the angular deflection amplitude of the drive mode, denoted as $\phi drive$ [rad]. On the right-hand side, the fluid mass flow rate $\Phi_m$, and the angular actuation frequency of the drive mode $\omega drive$ [rad/s] appear, normalized by the term $Ksense$ [N·m], which represents the structural elastic constant or torsional stiffness associated with the secondary sense mode. In experimental practice, the mass flow rate is measured by detecting the temporal phase shift between two geometrically symmetric points along the microchannel. In the absence of flow, the two points oscillate in perfect temporal phase, whereas, when the Coriolis force arises, the structure undergoes an asymmetric deformation that introduces a phase difference linearly correlated with the mass flow rate.

An alternative approach to make the measurement intrinsically independent of density variations of the medium consists in computing the net time delay, defined by the following Equation 1.3:

$$\tau = \frac{\Delta\theta}{2 \cdot \pi \cdot f_0} \tag{1.3}$$

where the variable $\tau$ [s] represents the absolute time delay, $\Delta\theta$ [rad] denotes the phase shift measured between the two sampling nodes, and $f_0$ [Hz] identifies the natural resonance frequency of the structural system, allowing the comparison of fluids with different properties without the need for repeated recalibration of the instrument.

In addition to flow rate quantification, the CMFS simultaneously operates as a high precision densimeter by exploiting variations in the natural resonance frequency of the

mechanical structure. The resonance frequency $f_0$ of the drive mode is analytically defined by the following Equation 1.4:

$$f_0 = \frac{1}{2\pi} \cdot \sqrt{\frac{k_D}{m_{ch} + \rho \cdot V_{ch}}} \tag{1.4}$$

where $k_D$ [N·m] represents the elastic constant or mechanical stiffness associated with the drive mode, $m_{ch}$ [kg] denotes the intrinsic mass of the empty channel structure, the variable $\rho$ [kg/m$^3$] expresses the mass density of the fluid under test, and $V_{ch}$ [m$^3$] defines the total internal geometric volume enclosed by the microchannel walls, whose product with the density yields the net mass of the contained fluid. Since the oscillation frequency is inversely proportional to the square root of the total resonator mass, given by the sum of the structural mass and the mass of the flowing fluid in the denominator, an increase in liquid density leads to a measurable decrease in $f_0$, enabling the extraction of the sample density with high metrological accuracy. In calibrated and thermally controlled systems, this accuracy can reach resolutions below one hundred parts per million (ppm) [13].

### 1.2.1 Actuation and sensing systems reported in the literature

The metrological performance of a MCMFS is inherently linked to the efficiency of its transduction subsystems, which must ensure stable excitation of the drive mode and ultra precise detection of the infinitesimal deflections induced in the sense mode. In the scientific literature, actuation strategies have historically focused on two main physical principles, namely the magnetomechanical effect based on the Lorentz force and the piezoelectric effect, each characterized by specific integration constraints and performance trade-offs. Lorentz force actuation (Figure 1.8), widely reported in SU-8 polymer-based devices developed by Monge et al. [1] and in surface silicon architectures developed by Haneveld et al. [2], is based on the interaction between an alternating electrical current flowing through metal traces deposited along the perimeter of the suspended channel and a static magnetic field generated by permanent magnets placed externally with respect to the chip. The resulting deflection force $\overrightarrow{F_L}$ is governed by the following physical law (Equation 1.5):

$$\overrightarrow{F_L} = I \cdot \left(\vec{L} \times \vec{B}\right) \tag{1.5}$$

where $\overrightarrow{F_L}$ [N] represents the actuation force vector, $I$ [A] denotes the alternating current intensity, $\vec{L}$ [m] defines the geometric vector corresponding to the length of the conductive trace exposed to the magnetic field and $\vec{B}$ [T] expresses the magnetic flux density vector of the external static field.

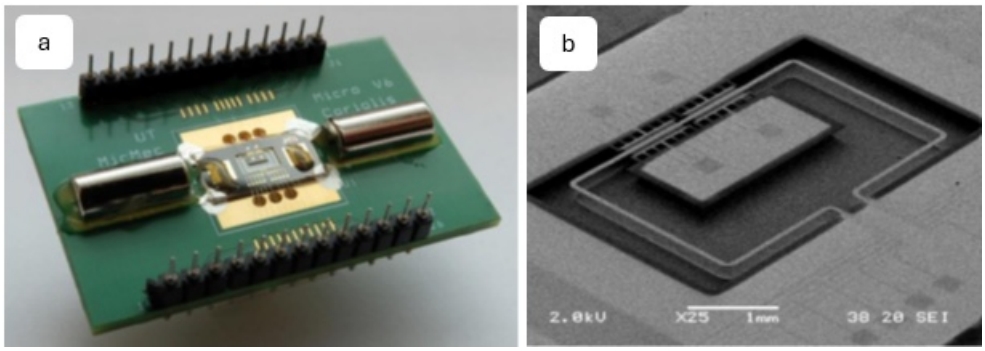


*Figure 1.8. (a) Sensor with electrical connections and permanent magnets for Lorentz force actuation. (b) Scanning electron microscope (SEM) image of the complete sensor [2].*

Although this approach enables the generation of large oscillation amplitudes with low driving voltages, the injection of electrical currents into microscale conductors inevitably induces parasitic self-heating due to Joule heating, which locally alters the rheological properties of the flowing fluid and causes thermal drifts in the elastic modulus of the structural material, thereby degrading device stability. To overcome this limitation, more recent developments reported by Zeng et al. [12] introduce piezoelectric actuation systems through the deposition of thin PZT films on the channel shell (Figure 1.9), where the application of an alternating electric field generates high impedance inverse mechanical deformation, eliminating thermal dissipation along the channel and enabling selective excitation of both symmetric flexural modes and asymmetric torsional modes with virtually negligible power consumption.

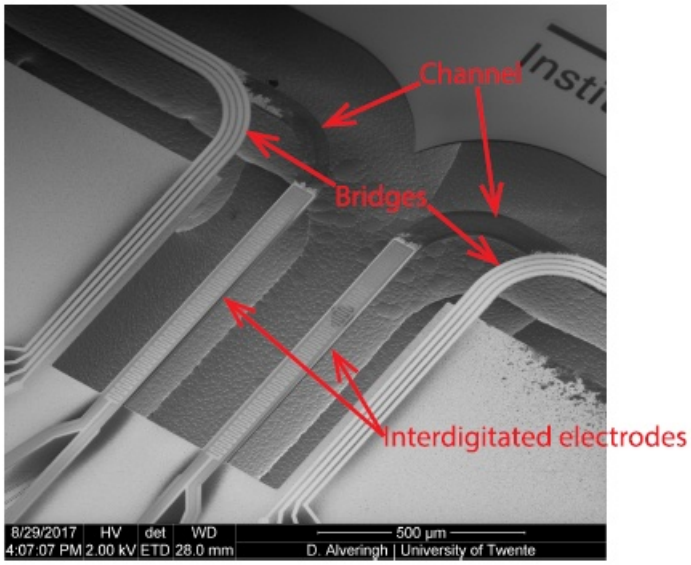


*Figure 1.9 SEM image of thin film PZT piezoelectric actuators integrated on the microfluidic channel [12].*

In order to experimentally validate the dynamic response of the microsensor without introducing the complexities associated with the microfabrication of active films, a preliminary actuation strategy based on a macroscale bulk piezoelectric actuator was adopted in this thesis work. The device support was directly bonded to the piezoelectric element, which was electrically driven by a function generator using a sinusoidal signal with controlled frequency and amplitude, thereby transmitting mechanical oscillations to the SU-8 architecture. This approach enabled a preliminary dynamic characterization to

identify the natural resonance frequencies of the microresonator and to study its sensitivity to mass variations induced by the introduction of fluids with known density. Based on the promising results obtained, future developments of the device will involve the integration of a chip level actuation system through the direct deposition of thin piezoelectric films onto the polymeric shell of the microsensor.

In parallel, the readout systems reported in the literature are mainly classified into optical, capacitive, and semiconductor integrated transduction schemes. Early bulk silicon resonators, such as those presented by Enoksson et al. [11], employed optical readout systems based on slots coupled with laser diodes and external photodetectors (Figure 1.10), a technique that is immune to electromagnetic interference but limited by large device footprints and alignment complexity, which prevent its use in portable systems.

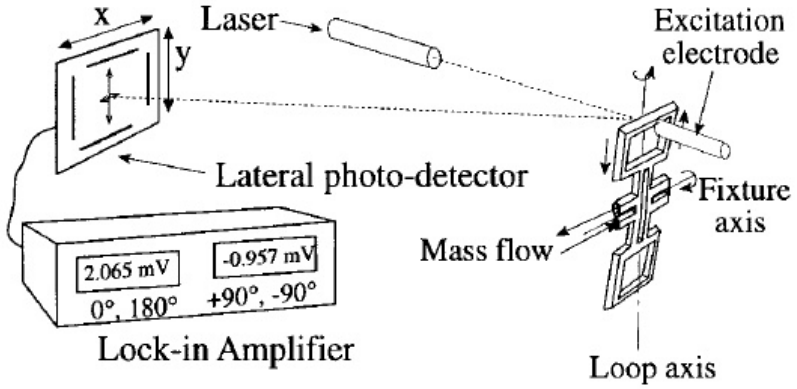


*Figure 1.10 Schematic of the measurement system with electrostatic actuation and optical detection of vibrations induced by the Coriolis force [11].*

Further downscaling has promoted the widespread adoption of differential capacitive readout, based on the use of interdigitated comb-finger electrodes (Figure 1.11) placed on both sides of the suspended channel [2, 4].

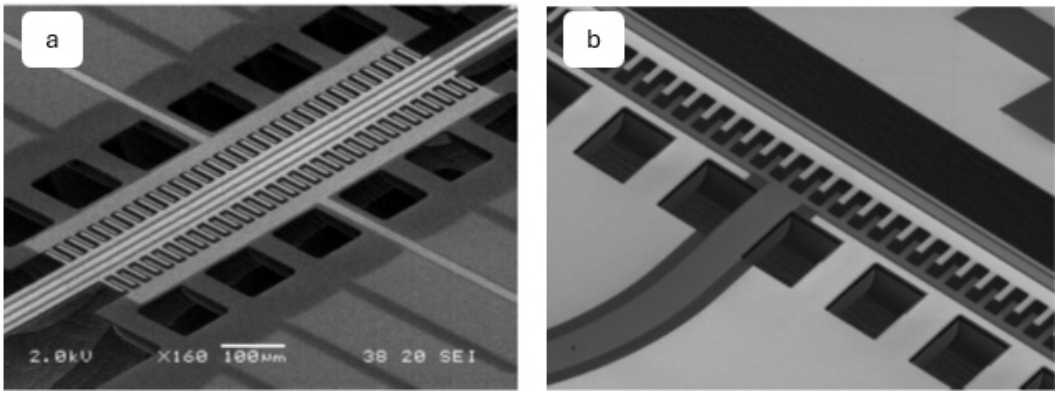


*Figure 1.11 (a) Detail of the comb-finger capacitive readout structure for measuring the actuation amplitude. (b) Detail of the comb-finger capacitive readout structure for measuring the response induced by the Coriolis force [2, 4].*

The net capacitance variation $\Delta C$ [F] induced by the mechanical phase shift of the sense mode is analytically modeled by the following Equation 1.6:

$$\Delta C = \varepsilon_0 \cdot \varepsilon_r \cdot \frac{N \cdot A}{d_0 \pm \Delta x} \tag{1.6}$$

where $\varepsilon_0$ [F/m] and $\varepsilon_r$ represent the permittivity of free space and the relative permittivity of the intervening medium, respectively, $N$ identifies the total number of coupled interdigitated fingers, $A$ [$m^2$] denotes the geometric overlap area between fixed and movable electrodes, $d_0$ [m] represents the nominal interelectrode gap distance, and $\Delta x$ [m] corresponds to the dynamic linear displacement induced by the Coriolis force, whose sign describes the differential approach or separation of the electrodes. Capacitive readout offers sub-nanometer resolution but is strongly affected by viscous damping generated by the compressed air film between the electrode surfaces during out of plane oscillation. This phenomenon, analyzed by Zeng et al. [12], significantly reduces the quality factor of the microresonator and requires the use of expensive vacuum packaging to preserve device sensitivity, thereby driving research toward either the fluid dynamic optimization of polymeric channel geometries or the integration of CMOS-based digital converters directly interfaced with the sensor in order to maximize the signal to noise ratio and mitigate parasitic capacitances from external connections [4].

# 2 Materials and methods

This chapter describes the microfabrication protocol of the Coriolis sensor and the experimental setup used for its dynamic characterization, as well as the selection of the employed material [14]. The structure of the microresonator is fabricated using SU-8 100 negative epoxy resin [8], whose high viscosity enables the formation, via a single spin coating step, of homogeneous films with thicknesses exceeding 200 µm, required to define the hydraulic cross-section of the microchannels. The cleanroom process flow [15] consists of a sequence of substrate pre-treatment steps [16, 17, 18, 19], deposition [20], soft bake, exposure [9], and PEB. After chemical development in solvent (propylene glycol monomethyl ether acetate, PGMEA [21]) to remove the unexposed polymer, the resulting geometries are verified using a profilometer [22]. Hermetic sealing of the channel is achieved via thermocompression SU-8 to SU-8 bonding [10], and the structural quality of the bonding is assessed through optical microscopy inspection [23] and fluidic tests [24] using a resin-based support [25]. The subsequent dynamic characterization employs a piezoelectric actuator support driven by a function generator with sinusoidal signals, which mechanically excites the device to map the resonance frequency shift as a function of the fluid density of the confined liquids. The dynamic response of the microchannel is monitored and quantified using a laser Doppler vibrometer (LDV) [26, 27].

## 2.1 SU-8 100 photoresist properties

SU-8 photoresist is a negative tone, chemically amplified polymer based on the commercial epoxy resin EPON® SU-8 and doped with a triarylsulfonium salt acting as a cationic photoinitiator (photoacid generator, PAG) [28, 29]. The specific formulation considered in this work, SU-8 100 (Kayaku Advanced Materials), is characterized by a high kinematic viscosity, which enables the formation of thicknesses exceeding 100 µm in a single spin coating process [8]. The transition of SU-8 from a viscous fluid to a 3D polymer network occurs through two successive stages. During UV exposure, typically at a wavelength of 365 nm, the photoinitiator decomposes, generating a strong Lewis acid that triggers the cross-linking process (Figure 2.1) [3, 30]. In the subsequent PEB step, thermal energy activates the acid catalyzed ring opening polymerization of the epoxy

groups. Since each molecule contains on average eight functional sites, a polymer network with high cross-linking density is formed [28]. Once fully cross-linked, SU-8 100 exhibits a glass transition temperature ($T_g$) above 200 °C[1] and high chemical resistance to most common organic solvents, as well as to strong acids and bases [8, 31].

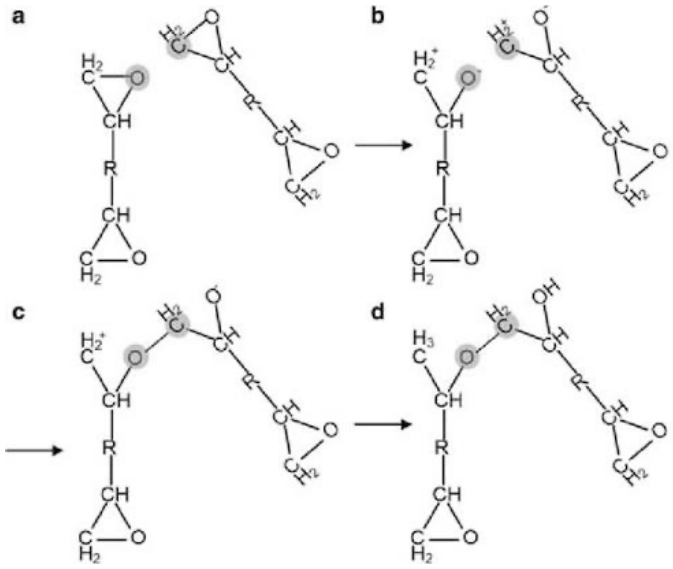


*Figure 2.1 Schematic representation of the SU-8 cross-linking process: (a) identification of reactive atoms within the reaction radius; (b) opening of the epoxide groups; (c) formation of cross-links through new covalent bonds; (d) hydrogen saturation of the remaining unreacted atoms [30].*

Once cross-linking is complete, the material exhibits a Young's modulus in the range of 3.5 GPa and 4.5 GPa, a tensile strength of (50 to 80) MPa, and a Poisson's ratio of approximately 0.33 [31, 32]. However, the volumetric shrinkage associated with curing and the mismatch in the CTE with respect to the substrate may generate residual stresses responsible for cracking and delamination phenomena [31].

From an optical perspective, SU-8 100 is highly transparent in the visible and near-infrared range ($\lambda > 400$ nm), while it exhibits strong absorption below 360 nm due to the

[1] In accordance with manufacturer guidelines [8, 36] and thermo-mechanical literature [31], the glass transition temperature ($T_g$) of SU-8 is not an intrinsic property of the commercial formulation but depends on the achieved degree of cross-linking. The maximum value (200 °C) is reached only after a complete hard bake process.

presence of the photoinitiator [2]. This property enables uniform penetration of UV radiation at 365 nm and the fabrication of high-aspect-ratio structures with nearly vertical sidewalls [3, 8].

Furthermore, when properly subjected to thermal stabilization treatments, the material becomes chemically inert and compatible with microfluidic and lab-on-chip applications, significantly reducing the presence of solvent and photoinitiator residues that could potentially leach into the fluid [1, 3].

During the process optimization in the cleanroom, the performance of SU-8 100 (Kayaku) was compared with that of SU-8 50 and SU-8 2100 formulations from the same family, belonging to the SU-8 2000 series and based on cyclopentanone as solvent [3, 8]. The comparison highlighted significant differences both in thermal cycling response and in bonding behavior.

Preliminary tests showed that SU-8 100 is particularly sensitive to thermal gradients. In the absence of controlled heating ramps during soft bake and PEB steps, the material tends to develop microcracks due to the accumulation of tensile stresses. In contrast, SU-8 2100 exhibited higher resistance to thermal shock, tolerating faster temperature variations without crack formation. Significant differences were also observed during sample pre-alignment prior to bonding: while SU-8 2100 required approximately 20 min at 120 °C to reach sufficient interface stability, SU-8 100 achieved stable preliminary adhesion after only 8 min at 100 °C. This behavior was further improved by introducing a Kapton layer as a structural support during processing.

SU-8 50 was progressively excluded from subsequent experimental activities as it is not suitable for the fabrication of structures thicker than 100 μm. The material also exhibited a strong tendency to warp after development, higher mechanical fragility, and yellowing effects after bonding. Although satisfactory joints could be achieved at temperatures between (170 and 190) °C and pressures between (1000 and 2000) N, these limitations discouraged its use in the present work. SU-8 2100, on the other hand, required particularly severe processing conditions, with temperatures close to 200 °C and loads between (800 and 2000) N.

Despite its higher sensitivity to thermal stress, SU-8 100 demonstrated a significant technological advantage during bonding operations. Experimental results showed that this formulation promotes molecular diffusion and interfacial adhesion between polymer surfaces at substantially lower temperatures compared to the other formulations analyzed.

This allowed sealing between base and cover layers to be performed at temperatures between (100 and 145) °C, applying loads ranging from (66 to 450) N over a reduced time interval of approximately 2 min.

Considering the experimental results, SU-8 100 (Kayaku) was identified as the most suitable formulation for the present study. The ability to operate at reduced temperature, time, and load during bonding minimized the risk of microfluidic channel collapse, limited material degradation, and improved process robustness, reproducibility, and throughput.

Table 2.1 compares the main characteristics of the SU-8 formulations used in the present thesis work.

*Table 2.1 Comparative overview of thermal and structural properties and optimal processing parameters during pre-bonding and bonding stages for SU-8 50, SU-8 2100, and SU-8 100 formulations.*

| | ***Bonding parameters*** | | | | |
|---|---|---|---|---|---|
| ***SU-8*** | ***T* [°C]** | ***F* [N]** | ***t* [min]** | **Pre-alignment** | **Notes** |
| ***50*** | from 170 to 190 | from 1000 to 2000 | 8 | 20 min at 120 °C | Limited use. Satisfactory structural results; frequent thermal browning |
| ***2100*** | from 190 to 215 | from 800 to 2000 | 4 | 20 min at 120 °C | High thermal shock stability. Requires high temperature bonding |
| ***100*** | **from 100 to 145** | **from 66 to 450** | 2 | **8 min at 100 °C** | Optimal choice. Early activation of surface transitions; ultrafast bonding |

## 2.2 Substrate preparation and SU-8 deposition

The microresonator fabrication process began with the deposition of a sacrificial OmniCoat layer (Kayaku Advanced Materials, Inc.) [16, 33] on the supporting substrate, as illustrated in Figure 2.2. After a preliminary chemical cleaning step aimed at removing organic and particulate contaminants, the resist was applied by spin coating (Table 2.2) in amounts appropriate for the wafer size [33]. The OmniCoat layer plays a key role in the subsequent device release, facilitating the detachment of the microfabricated structures from the substrate at the end of the process.

*Table 2.2 Spin-coating conditions adopted for the deposition of the OmniCoat layer.*

| | ***Spin speed* [rpm]** | ***Acceleration* [rpm/s]** | ***Time* [s]** |
|---|---|---|---|
| ***Step 1*** | 500 | 100 | 5 |
| ***Step 2*** | 3000 | 300 | 30 |

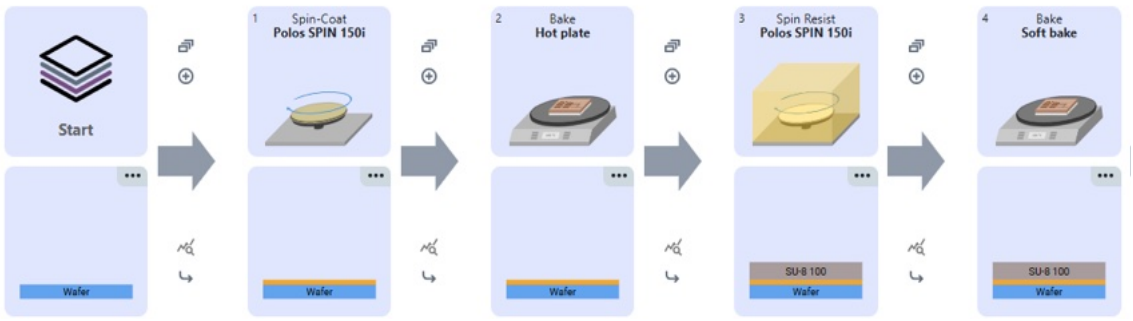


*Figure 2.2 Sequence for the preparation of the first base layer of the device. Schematic prepared using FabuBlox.*

On top of the OmniCoat layer, the SU-8 100 photoresist was subsequently deposited using a spin coater. The formulation, characterized by high viscosity at room temperature, required careful optimization of the spin coating parameters to ensure uniform thickness and film quality [8]. The parameters used for the different layers are reported in Tables 2.3 and 2.4.

*Table 2.3 Spin coating deposition parameters of SU-8 100 for the first base layer and cover layer.*

| | ***Spin speed* [rpm]** | ***Acceleration* [rpm/s]** | ***Time* [s]** |
|---|---|---|---|
| ***Step 1*** | 500 | 200 | 10 |
| ***Step 2*** | 2000 | 200 | 60 |

*Table 2.4 Spin coating deposition parameters of SU-8 100 for the fabrication of the microchannels (second base layer).*

| | ***Spin speed* [rpm]** | ***Acceleration* [rpm/s]** | ***Time* [s]** |
|---|---|---|---|
| ***Step 1*** | 500 | 200 | 10 |
| ***Step 2*** | 6000 | 200 | 30 |

The high viscosity of the material enables the fabrication of thick and mechanically robust structures but may lead to edge bead formation and air bubble entrapment within the film [3, 8]. To minimize these defects, a soft bake step was performed on a hotplate after deposition. The thermal cycle consisted of a first controlled heating ramp, with an increase rate of 5 °C/min from room temperature up to 65 °C, where the sample was held for 10 min. Subsequently, a second ramp with the same slope was applied up to 95 °C, at which temperature the sample was maintained for 30 min for 100 µm thick films and 20 min for 50 µm thick films [8]. This treatment enabled gradual evaporation of the gamma-butyrolactone (GBL) solvent, reducing the risk of residual stress and cracking phenomena and stabilizing the film prior to subsequent processing steps.

## 2.3 Laser direct writing exposure and chemical development of the photoresist

The correct geometrical definition of the suspended fluidic channels of the Coriolis microresonator represents one of the most critical steps in the entire microfabrication process. Based on the state of the art and the available research literature, the initial strategy involved the use of conventional UV photolithography through a Mask Aligner NQX 4006 [1, 34]. However, preliminary laboratory tests revealed significant physical limitations related to the intrinsic behavior of SU-8 100 when deposited in very thick films. The lack of perfect surface planarity of the resist and light diffraction phenomena within the polymer layer led to a loss of resolution. To overcome these issues and optimize the process, the strategy was modified by abandoning the physical mask in favor of LDW technology [35]. This transition was implemented using the Heidelberg DWL 66+ industrial system, an advanced machine that focuses a laser beam and scans it point by point directly on the photoresist following the digital computer-aided design (CAD) layout [9]. As shown in recent studies on the optimization of exposure of thick SU-8 films using DWL systems, the elimination of the hard mask allows modulation of both energy dose and laser focus position through the film thickness, enabling nearly perfectly vertical sidewalls and eliminating contact related optical defects [35]. This flexibility enabled the rapid development and testing of five different geometric design versions of the digital masks directly in the laboratory, optimizing geometries and alignment tolerances before converging to the final sensor configuration.

From a chemical standpoint, the targeted laser irradiation activates the photoinitiator within SU-8 100, generating a photo-induced acid exclusively in the exposed regions [8]. To complete the material transformation, immediately after exposure the wafer undergoes a PEB, which is essential to provide the thermal energy required to trigger 3D cross-linking and render the polymer fully insoluble [8]. The process flow diagram for the fabrication of the complete device base is reported below, starting from the first SU-8 layer previously obtained (Figure 2.3). For the fabrication of the covers, the process is analogous but was stopped after the first PEB step, followed directly by the development stage.

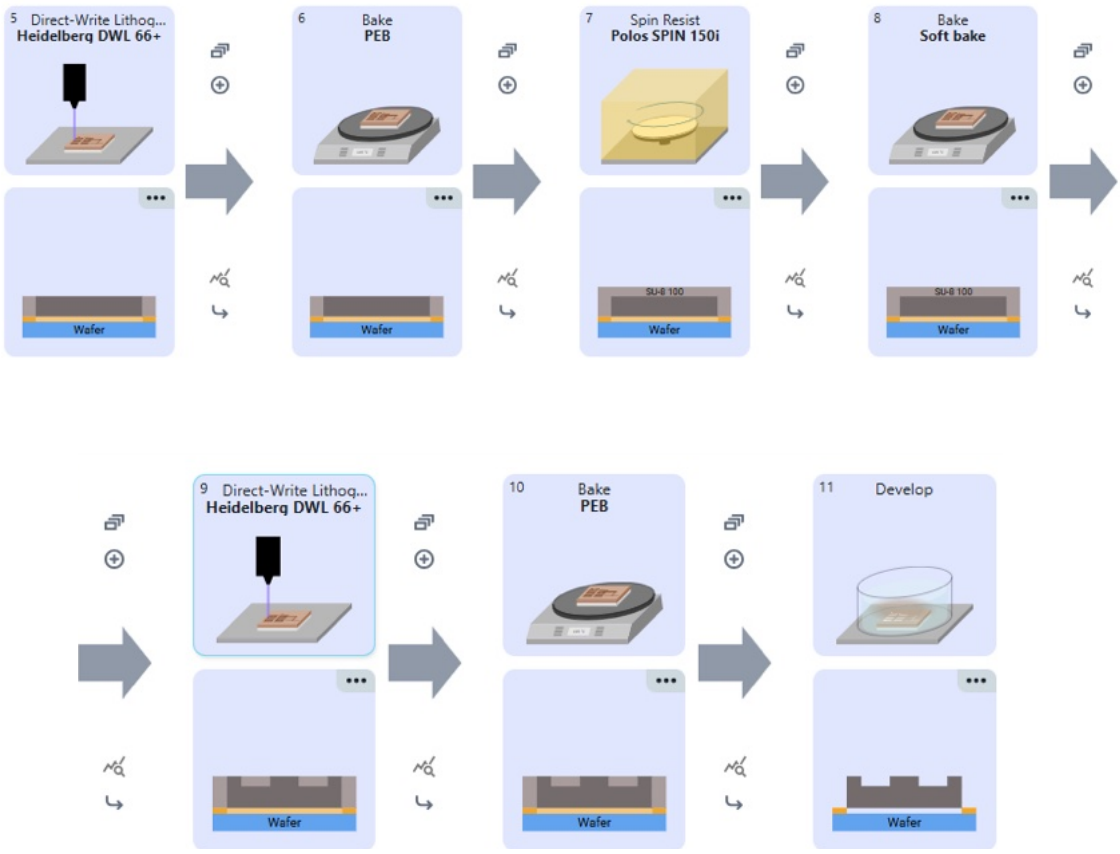


*Figure 2.3 Process flow for the fabrication of the complete device bases starting from the first SU-8 layer. Schematic prepared using FabuBlox.*

In order to ensure the structural integrity of the device, the thermal treatment was carried out in a progressive manner on a hotplate, to limit the onset of internal mechanical stresses and prevent polymer cracking. The cycle consisted of a first controlled heating ramp, with an increase rate of 5 °C/min from room temperature up to 65 °C, followed by a holding time of approximately 1 min. Subsequently, a second ramp with the same slope was applied up to 95 °C. The dwell time at this temperature depends on the thickness of the deposited film and was set to 10 min for 100 µm thick layers used in channel definition and to 5 min for thinner 50 µm layers [8].

Once the thermal curing step was completed and the substrate was cooled down, selective removal of the non-exposed SU-8 was performed through a wet development process lasting 12 min in PGMEA followed by an immediate rinse in isopropyl alcohol (IPA) to remove residual unexposed resist [8]. PGMEA dissolved the uncross-linked resist, enabling the formation of the microchannels and the etching of the sacrificial OmniCoat layer required for the subsequent device release [33]. All quantitative parameters of these procedures are summarized for convenience in Table 2.5.

*Table 2.5 Process sequence for the fabrication of SU-8 device bases.*

## Process flow

### Base layer 1

**Substrate stack:**

**Wafer:** 1000 nm, 4 inches

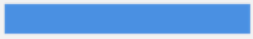

Step 1:

**Tool name:** Polos SPIN 150i
**Name:** Spin resist
**Resist:** OmniCoat
**Resist type:** Lift-off resist (LOR)

**Step 1**
**Acceleration:** 100 rpm/s
**Spin speed:** 500 rpm
**Spin time:** 5 s

**Step 2**
**Acceleration:** 300 rpm/s
**Spin speed:** 3000 rpm
**Spin time:** 30 s

Step 2:

**Tool name:** Hot plate
**Name:** Bake
**Bake temperature:** 200 °C
**Bake time:** 1 min

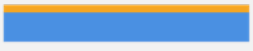

Step 3:

**Tool name:** Polos SPIN 150i
**Name:** Spin resist
**Resist:** SU-8 100
**Resist type:** Negative
**Film thickness:** 100 µm

**Step 1**
**Acceleration:** 200 rpm/s
**Spin speed:** 500 rpm
**Spin time:** 10 s

**Step 2**
**Acceleration:** 200 rpm/s
**Spin speed:** 2000 rpm
**Spin time:** 60 s

Step 4:

**Tool name:** Hot plate
**Name: Bake**: soft bake
**Bake temperature:** 65 °C
**Bake time:** 10 min
**Temperature ramp:** 5 °C/min
**Bake temperature:** 95 °C
**Bake time:** 30 min

Step 5:

**Tool name:** Heidelberg DWL 66+
**Name:** Direct-write lithography
**Laser power:** 30 mW
**Intensity:** 100%
**Filter:** 100
**Focus offset:** -100, 0, 100

Step 6:

**Tool name:** Hot plate
**Name: Bake:** PEB
**Bake temperature:** 65 °C
**Bake time:** 1 min
**Temperature ramp:** 5 °C/min
**Bake temperature:** 95 °C
**Bake time:** 10 min

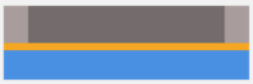

## Base layer 2

Step 7:

**Tool name:** Polos SPIN 150i
**Name:** Spin resist
**Resist:** SU8-100
**Resist type:** Negative
**Film thickness:** 50 µm

**Step 1**
**Acceleration:** 200 rpm/s
**Spin speed:** 500 rpm
**Spin time:** 10 s

**Step 2**
**Acceleration:** 200 rpm/s
**Spin speed:** 6000 rpm
**Spin time:** 30 s

Step 8:

**Tool name:** Hot plate
**Name:** Soft bake
**Bake temperature:** 65 °C
**Bake time:** 1 min
**Temperature ramp:** 5 °C/min
**Bake temperature:** 95 °C
**Bake time:** 5 min

Step 9:

**Tool name:** Heidelberg DWL 66+
**Name:** Direct-write lithography
**Laser power:** 30 mW
**Intensity:** 100%
**Filter:** 100
**Focus offset:** 0, 0

Step 10:

**Solution name:** PGMEA
**Name:** Develop
**Time:** 12 min

The fabrication of the cover followed a similar workflow to that adopted for the first SU-8 layer of the base, including spin coating, soft bake, UV exposure, post-exposure bake, and development. The complete fabrication process was concluded by aligning and thermally bonding the two components, as described in the following section.

## 2.4 Layout design in CleWin5 and geometric evolution of the design

The transfer of geometric patterns onto the photoresist requires the preliminary generation of a digital two-dimensional layout, performed using the CAD software CleWin5, which is employed for defining layouts in microfabrication. In the initial phase, the patterns were intended for the fabrication of photolithographic masks for exposure using a mask aligner. The subsequent adoption of the Heidelberg DWL 66+ system enabled a transition to LDW, simplifying the workflow, accelerating design iterations based on experimental results obtained in the cleanroom, and simultaneously improving the precision and geometric reproducibility of the fabricated devices (Figure 2.4).

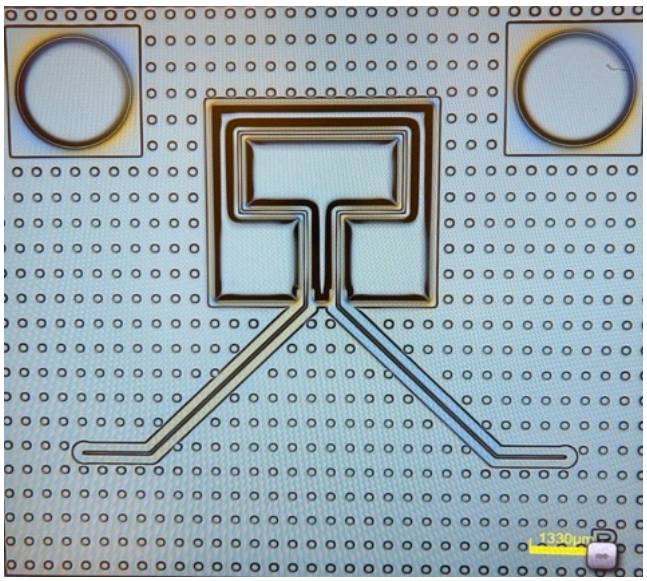


*Figure 2.4 Final version of the Coriolis microsensor layout obtained via LDW.*

The final configuration of the Coriolis microsensor is represented by version 5 (Figure 2.5), an optimized layout designed to maximize the mechanical robustness of the structure and the reliability of fluidic sealing. This revision introduces thickened microchannel walls, capable of withstanding mechanical loads up to 800 N and temperatures up to 150 °C. The design also incorporates enlarged structural pillars of 120 µm, localized reinforcements in the cantilever region of the Ω-shaped geometry, and

dedicated alignment marks to optimize laser writing and interlayer alignment. The achievement of this final configuration resulted from an iterative optimization process developed through five successive layout revisions, each introduced to address specific issues observed during fabrication, bonding, and device characterization.

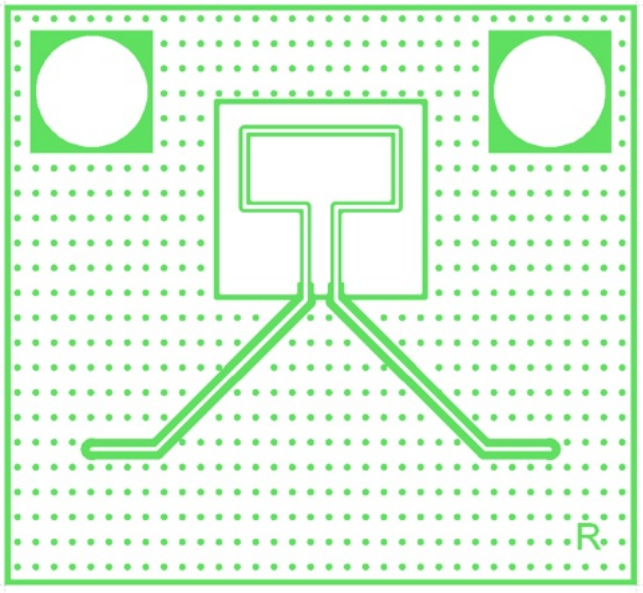


*Figure 2.5 Final microsensor layout (version 5) optimized for mechanical robustness and bonding.*

The starting point of this development, identified as version 1 and inherited from preliminary designs of the research group, featured 90 µm microchannels with straight walls and sharp corners. However, initial tests revealed chip warping and deformation phenomena induced by the development and release steps, leading to difficulties during bonding (Figure 2.6) [1, 4, 8]. This residual curvature compromised the uniformity of contact during bonding and made interlayer alignment particularly critical, hindering the achievement of homogeneous adhesion and proper device operation.

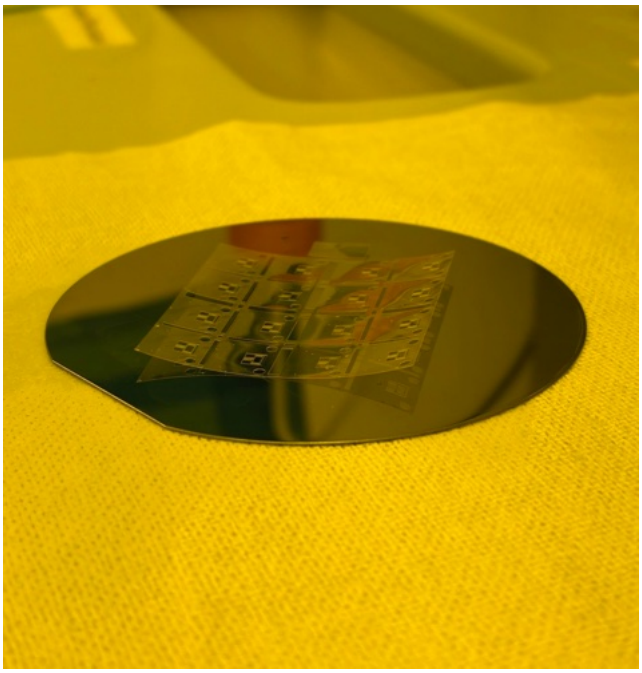

*Figure 2.6 Warpage resulting from the photoresist development process.*

To mitigate these issues, version 2 introduced two major innovations: on one hand, localized curved fillets were added at the most highly stressed junctions to minimize stress concentration phenomena (Figure 2.7); on the other hand, structural connectors were implemented (Figure 2.8). These polymer bridges, initially integrated only in the bottom layer and later extended to the covers as well, kept the chips mechanically linked during wet development, homogenizing release conditions and significantly reducing asymmetric deformation within the same wafer. Despite the improvement in planarity, version 2 still exhibited frequent failures due to microvoids and air pockets along the fluidic channels during the sealing phase.

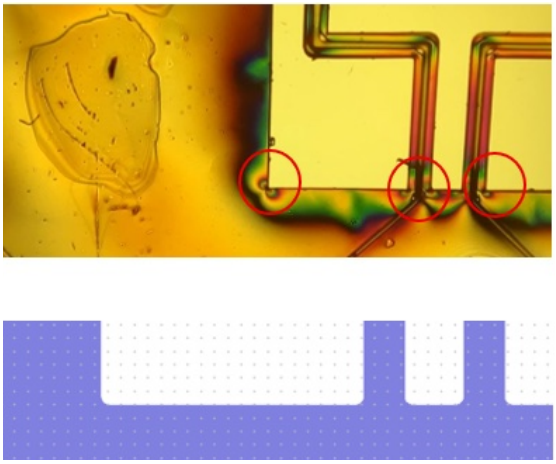

*Figure 2.7 Identification of stress concentration regions and implementation of curved fillets to reduce local stress accumulation.*

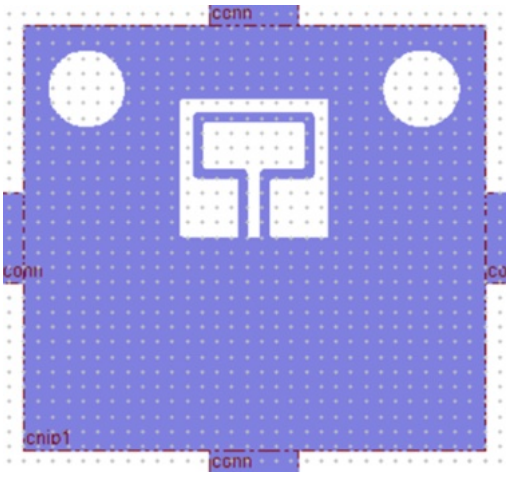


*Figure 2.8 Microsensor geometry with structural connectors used to keep devices mechanically constrained during development and handling steps.*

Version 3 attempted to improve bonding efficiency by modifying the second layer, restricting it to the microchannel region only in order to locally concentrate the compression pressure (Figure 2.9).

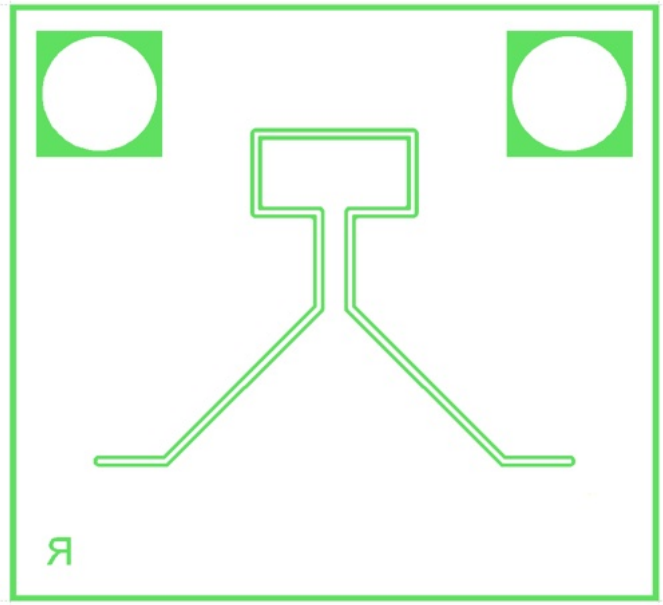

*Figure 2.9 Version 3 layout with a localized second-layer relief along the microchannel profile for bonding optimization.*

Although this approach was promising, experimental tests revealed the formation of vacuum pockets near the channels and a pronounced sensitivity to interlayer misalignment (Figure 2.10). These phenomena were attributed to the height mismatch between the raised channel region and the surrounding areas, which prevented the cover layer from plastically conforming during bonding, thereby promoting the formation of localized voids. This resulted in fluidic sealing issues and device delamination phenomena.

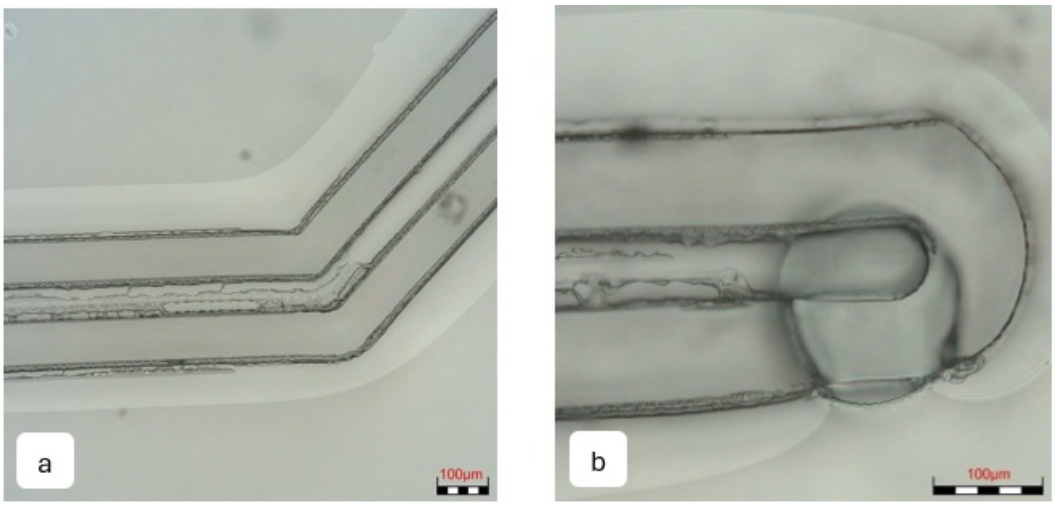


*Figure 2.10. (a) Void formation near the microchannels during the bonding process. (b) Misalignment between cover holes and microchannels in version 3 leading to reduced fluidic sealing performance.*

To overcome these limitations, version 4 introduced a dense distribution of 40 µm support pillars in the empty regions of the device (Figure 2.11), with the aim of interrupting the continuity of residual cavities and more uniformly distributing the bonding load.

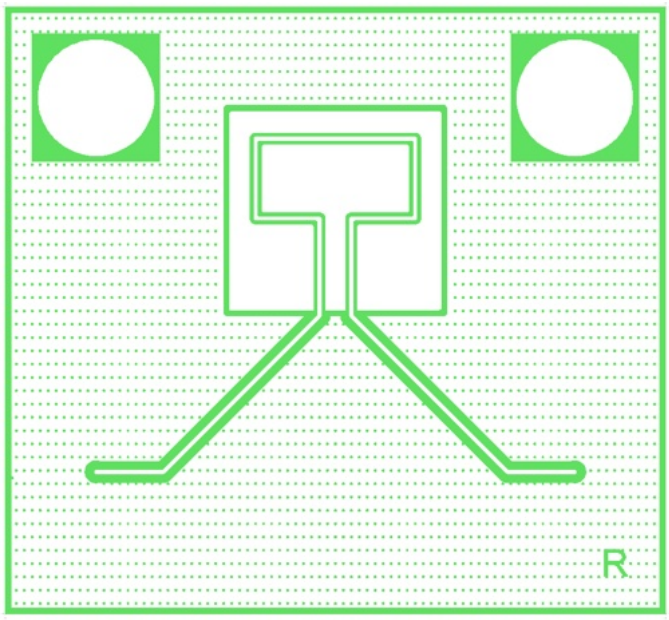


*Figure 2.11 Version 4 device featuring support pillars for bonding optimization.*

At the same time, the microchannel contours were widened (Figure 2.12) at the fluid inlet and outlet regions, increasing tolerance to interlayer misalignment. These modifications improved pressure distribution during bonding and reduced the risk of leakage.

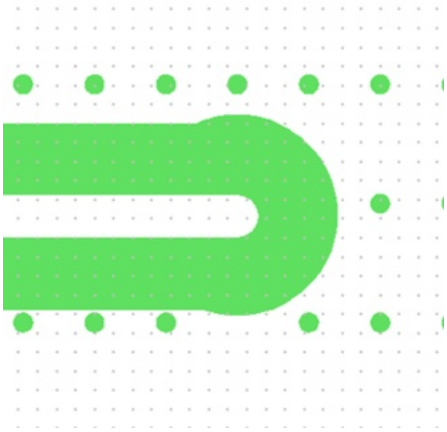

*Figure 2.12 Enlarged microchannel inlet and outlet regions to increase tolerance to misalignment.*

However, during mechanical characterization tests, the channel walls exhibited partial structural inadequacy under compression loads exceeding 1200 N. Beyond this threshold, SU-8 showed microcracking, plastic deformation, and, in the most severe cases, channel wall collapse. The 40 µm pillars also proved vulnerable under such conditions, undergoing fracture and generating polymer debris capable of migrating into the microfluidic circuit and obstructing the flow (Figure 2.13).

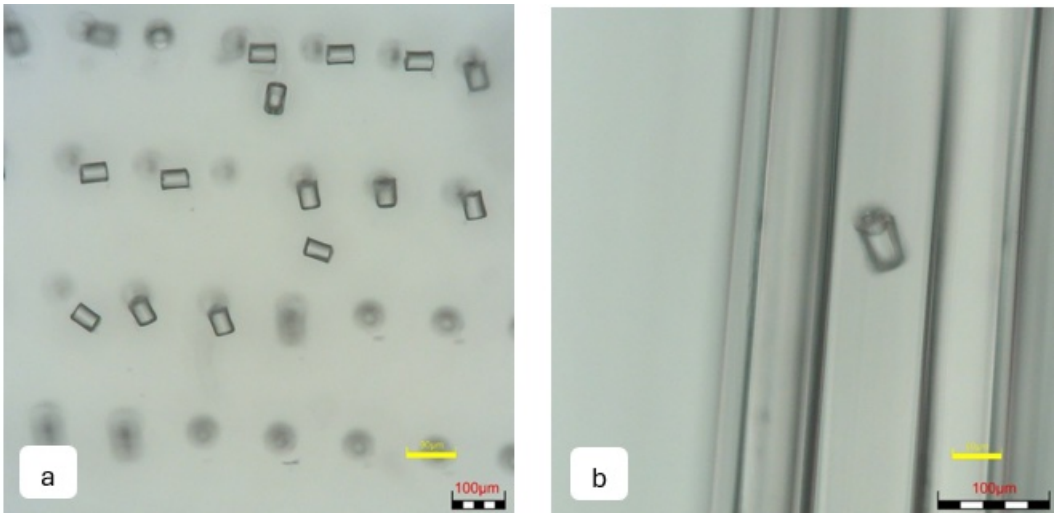


*Figure 2.13 (a) Structural failure of 40 µm support pillars. (b) Microchannel blockage caused by a detached pillar fragment.*

All these findings guided the development of version 5, establishing it as the final configuration of the microsensor. In this final revision, the wall thickness of the microchannels was progressively increased to withstand the high pressures required during bonding without inducing surface cracking phenomena, while the pillar diameter was increased up to 120 µm, with a corresponding reduction in spatial density and a significant improvement in compressive strength. To ensure device integrity during handling and release steps, version 5 incorporated specific structural reinforcements at the onset of the cantilevered section of the Ω-shaped structure, frequently prone to catastrophic failure (Figure 2.14a). These reinforcing elements were extended across all three layers of the sensor to improve mechanical robustness (Figure 2.14b).

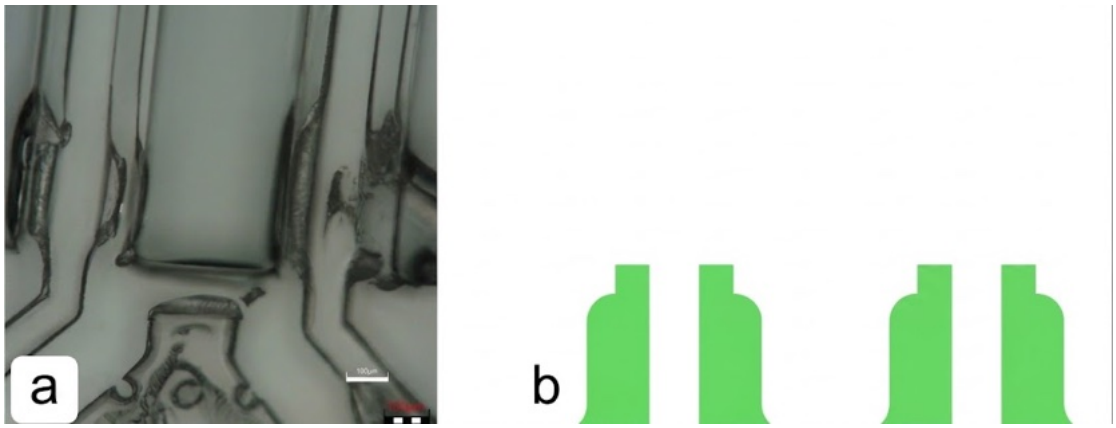


*Figure 2.14 Structural optimization of version 5: (a) typical catastrophic failure of the Ω-shaped cantilever; (b) reinforcing structures introduced and extended through all sensor layers.*

Finally, the introduction of dedicated centering systems and alignment marks (Figure 2.15), optimized for optical recognition by the DWL system, reduced interlayer coupling errors, enabling a configuration characterized by high mechanical robustness, uniform distribution of bonding pressures, and reduced delamination phenomena during fluidic tests.

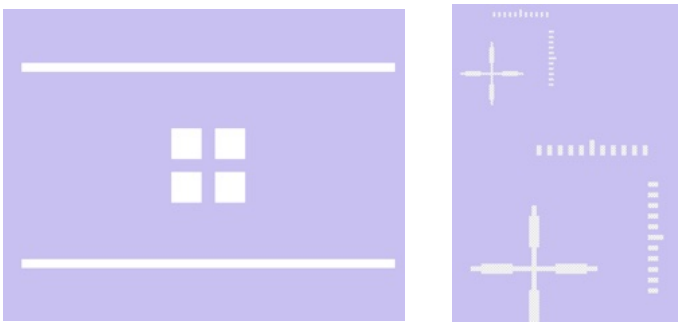

*Figure 2.15 Centering structures and alignment marks for improved inter-layer alignment in version 5.*

## 2.5 SU-8 to SU-8 thermocompression bonding sealing process

Hermetic sealing of the fluidic microchannels represents one of the most complex and critical steps in the microfabrication process of the Coriolis microsensor. The bonding between base and cover layers must ensure hydraulic tightness during operation while preserving both the channel geometry and its resistance to the mechanical stresses generated during actuation near the resonance frequency. Therefore, bonding quality directly affects both the structural reliability and the fluidic performance of the sensor.

To meet these requirements, a homogeneous SU-8/SU-8 bonding process was adopted, governed by the combined action of temperature and controlled pressure. The bonding mechanism is based on interdiffusion of polymer chains at the interface between the microchannel substrate and its corresponding cover [30]. The application of uniform pressure promotes intimate contact between the surfaces, while thermal input increases molecular mobility and enables completion of the cross-linking reactions of the remaining epoxy groups. The result is the formation of a continuous interface characterized by a stable bond.

From a technological standpoint, the process was carried out using an EVG 510 hot embossing system (Figure 2.16) [10], which allowed precise control of process parameters, thermal ramps, and a vacuum processing environment that reduces air entrapment at the layer interface, thereby limiting defect formation during bonding.


*Figure 2.16 EVG 510 thermocompression bonding system.*

The system is equipped with two independent heating plates (upper and lower), which allow the separate adjustment and control of thermal conditions during the bonding process. In all experimental tests, a controlled heating ramp of 20 °C/min was used, selected to reduce the onset of thermal stresses in the material and to ensure a more uniform temperature distribution within the large thicknesses of SU-8 100 [8].

Particular attention was also devoted to the cooling stage, since preliminary tests had shown that rapid thermal variations promoted the formation of cracks and the development of residual stresses in the polymer. For this reason, cooling was performed gradually inside the tool until a temperature of 50 °C was reached, thereby minimizing the effects associated with thermal shock.

The first optimization phase was dedicated to studying the influence of the bonding temperature, while keeping the applied force constant at 250 N (complete data are reported in Table 2.6). The choice of the investigated temperature range stems from observations made during the pre-alignment stage. Before the actual bonding process, the base and cover were brought into contact on a hotplate set to 120 °C (subsequently reduced to 100 °C) using a dedicated support in order to generate a temporary adhesion between the two layers (Figure 2.17). Although this adhesion is not permanent, it ensured the correct alignment of the geometries during subsequent handling and bonding operations. Given that partial interfacial adhesion was achieved at this pre-alignment temperature, the subsequent tests were set around this value, both toward lower conditions to identify the minimum activation threshold of the process and toward higher temperatures to determine the limit beyond which degradation or structural deformation phenomena began to occur.

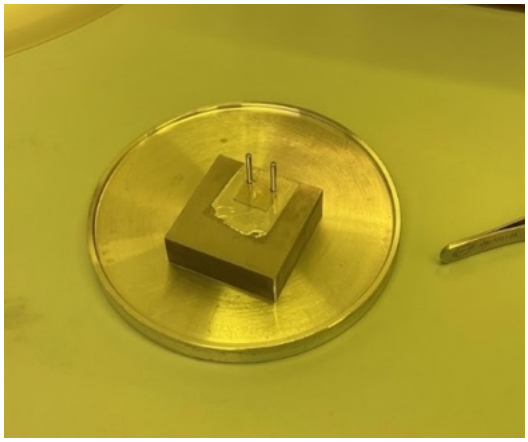

*Figure 2.17 Pre-alignment support for base and cover layers.*

The tests performed in the temperature range between 100 °C (sample 11) and 110 °C (sample 9) (Table 2.6) showed partial adhesion between the layers and incomplete interfacial interaction (Figure 2.18). By progressively increasing the temperature up to 125 °C, as observed in samples 6, 7, and 8, a significant improvement in bond quality was obtained, with the appearance of the first fully sealed and mechanically stable joints.

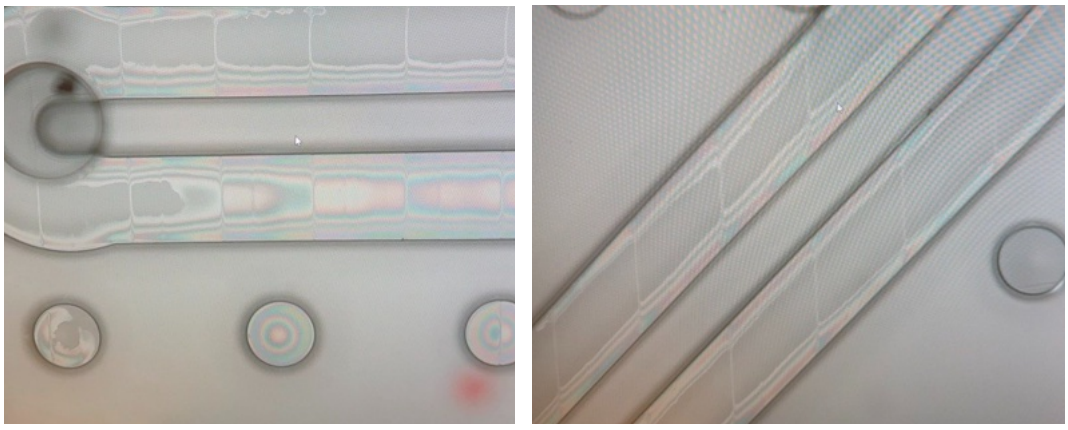

*Figure 2.18 Incomplete sealing of the microchannel due to insufficient thermocompression bonding.*

The best performance was obtained in the temperature range between (130 and 135) °C, corresponding respectively to sample 1 and sample 2, where the bonding exhibited high uniformity and good structural integrity. Under these conditions, the process ensured proper interfacial adhesion without significantly altering the geometry of the microchannels (Figure 2.19).

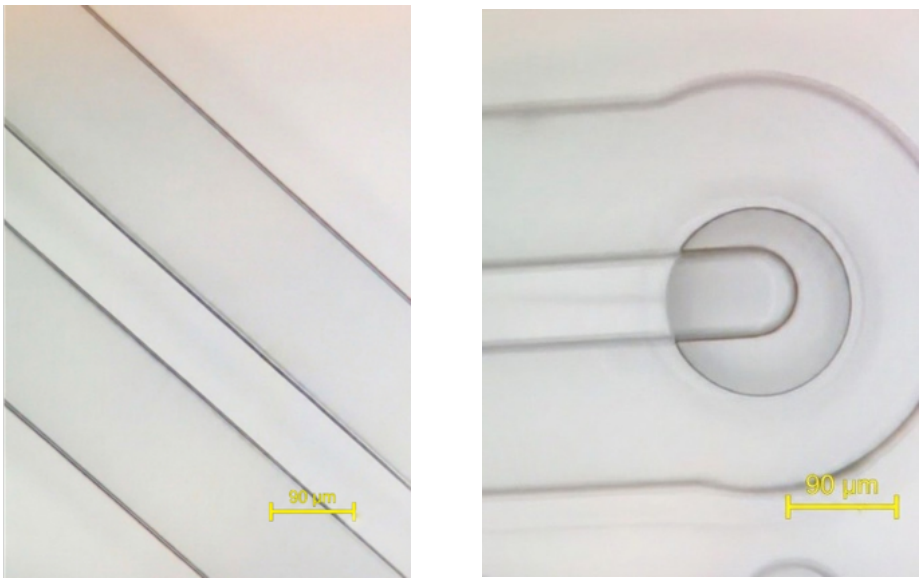


*Figure 2.19 Complete sealing of the microchannel achieved through optimized thermo-compression bonding.*

An increase in temperature above 140 °C, analyzed for samples 3, 4, and 5, instead revealed wall deformation phenomena, narrowing of the fluidic cross-sections, and, in the most critical cases, permanent alterations of the device geometry (Figure 2.20).

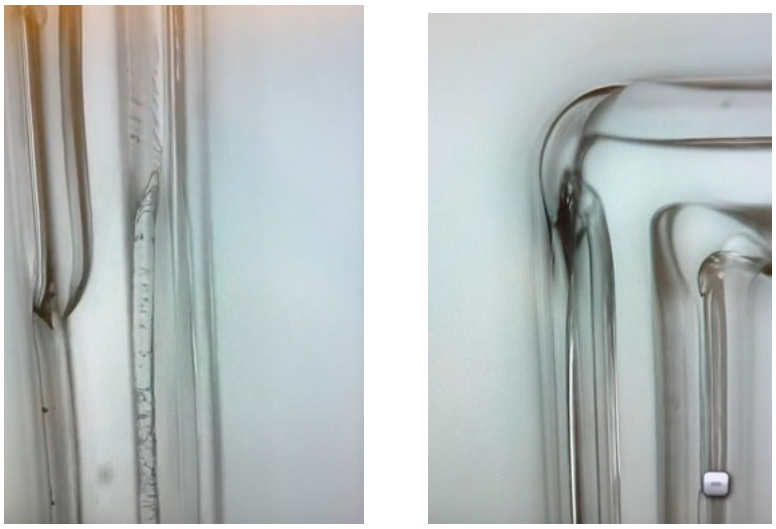

*Figure 2.20 Microchannel collapse caused by excessive bonding temperature.*

Once the most favorable temperature window had been identified, attention was directed toward the effect of bonding pressure. The experiments were conducted by varying the applied load between (280 and 480) N while maintaining the optimal temperature constant at 130 °C. The results showed that forces between (280 and 300) N, corresponding to samples 12 and 13, already provided good adhesion and satisfactory preservation of the device geometry. However, the most balanced performance was observed in the range between (320 and 400) N, corresponding to samples 14 and 15, where the best combination of bond quality, sealing uniformity, and microchannel geometric accuracy was achieved (Figure 2.21).

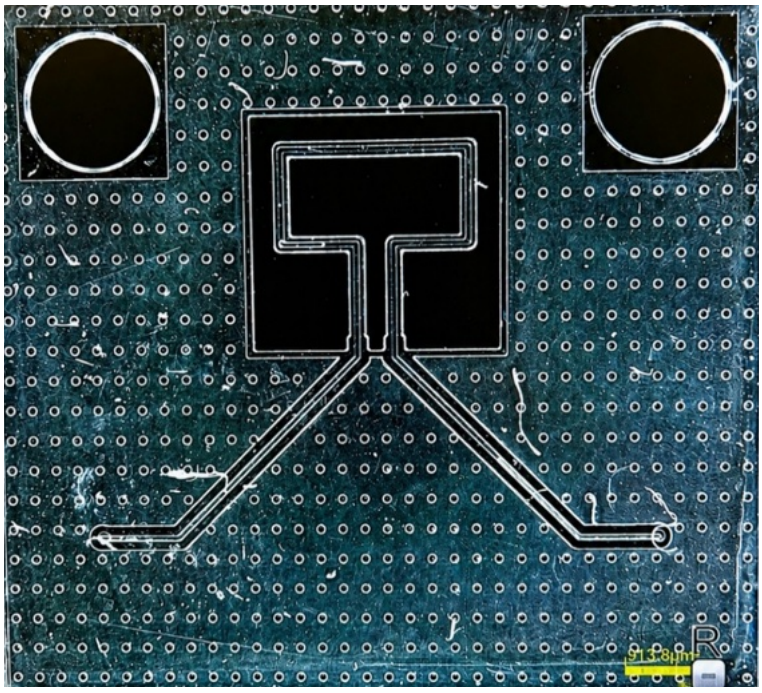

*Figure 2.21 Optical microscope image of sample 15, fabricated under thermocompression bonding conditions of 130 °C and 400 N, showing successful sealing of the Ω-shaped microchannel.*

The experiments also revealed that increasing pressure was generally less critical than increasing temperature. While temperature directly influenced the dimensional stability of the polymer structures, pressure mainly contributed to improving the interfacial contact between the base and the cover. Nevertheless, beyond a certain threshold, the mechanical load also produced detrimental effects. In particular, for forces of 480 N applied to samples 16 and 17, wall failure and immediate microchannel collapse were observed, thereby identifying the upper operational limit of the process.

Overall, the analysis allowed the definition of an optimal process window for the bonding of version 5, corresponding to temperatures between (125 and 135) °C and applied forces between (320 and 400) N. The effectiveness of these process conditions will be subsequently validated through the microfluidic tests and dynamic characterization experiments presented in Chapter 3.

*Table 2.6 Process parameters and experimental results of the SU-8/SU-8 thermocompression bonding experiments.*

| ***Test*** | ***Top/bottom T* [°C]** | ***Time* [min]** | ***F* [N]** | ***T ramp* [°C/s]** | ***F ramp* [N/s]** | ***N° chip*** | ***Comments*** |
|---|---|---|---|---|---|---|---|
| ***1*** | 130/130 | 2 | 250 | 20 | 50 | 1 | Sufficient T, insufficient F |
| ***2*** | 135/135 | 2 | 250 | 20 | 50 | 1 | Excellent result |
| ***3*** | 140/140 | 2 | 250 | 20 | 50 | 1 | Channel deformation and collapse observed. Very good bonding, but worse overall than the previous test |
| ***4*** | 145/145 | 2 | 250 | 20 | 50 | 1 | Deformed but intact and well bonded. Minor burning signs |
| ***5*** | 150/150 | 2 | 250 | 20 | 50 | 1 | Severe burning and channel collapse observed |
| ***6*** | 125/125 | 2 | 250 | 20 | 50 | 1 | Excellent result |
| ***7*** | 120/120 | 2 | 250 | 20 | 50 | 1 | Bonded successfully. Not optimal, but sufficient for flow testing |
| ***8*** | 115/115 | 2 | 250 | 20 | 50 | 1 | Good bonding |
| ***9*** | 110/110 | 2 | 250 | 20 | 50 | 1 | Good bonding |
| ***10*** | 105/105 | 2 | 250 | 20 | 50 | 1 | Sufficient bonding |
| ***11*** | 100/100 | 2 | 250 | 20 | 50 | 1 | Sufficient bonding |
| | | | ***Force variation tests at 130 °C.*** | | | | |
| ***12*** | 130/130 | 2 | 280 | 20 | 80 | 1 | Good bonding |
| ***13*** | 130/130 | 2 | 300 | 20 | 90 | 1 | Good bonding |
| ***14*** | 130/130 | 2 | 320 | 20 | 100 | 1 | Excellent result |

| | | | | | | | |
|---|---|---|---|---|---|---|---|
| ***15*** | 130/130 | 2 | 400 | 20 | 120 | 1 | Excellent result |
| ***16*** | 130/130 | 2 | 480 | 20 | 150 | 1 | Channel collapse observed |
| ***17*** | 120/120 | 2 | 480 | 20 | 150 | 1 | Channel collapse observed |

***Multi-sample tests.***

| | | | | | | | |
|---|---|---|---|---|---|---|---|
| ***18*** | 125/125 | 2 | 400 | 20 | 120 | 4 | Excellent result |
| ***19*** | 130/130 | 4 | 500 | 20 | 80 | 2 | Good bonding, slight deformation |
| ***20*** | 135/135 | 4 | 430 | 20 | 70 | 2 | Good bonding, slight deformation |
| ***21*** | 130 | 8 | 500 | 20 | 70 | 2 | Good bonding, slight deformation |

During the optimization of the bonding process, it was observed that the success of the joint depends critically on both the quality of the pre-alignment procedure and the cleanliness of the interfacing surfaces. Even minor misalignments during the preliminary stage at 120 °C resulted in an asymmetric pressure distribution during compression, leading to localized collapse of the microchannels. A high sensitivity to particulate contamination was also observed: the presence of particulate matter at the bonding interface hinders intimate contact between the layers, resulting in reduced sealing uniformity and an increased likelihood of localized delamination (Figure 2.22).

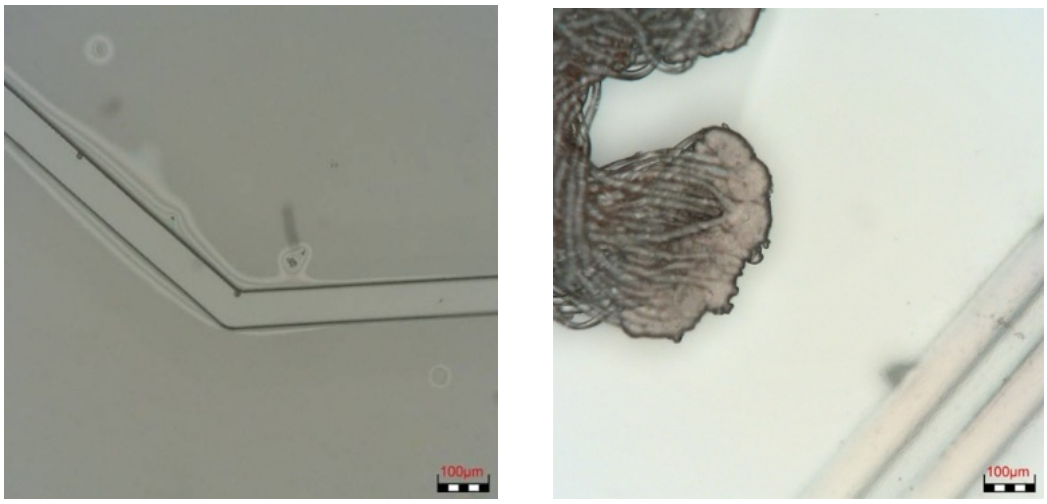


*Figure 2.22 Local delamination caused by contaminants trapped at the interface during the bonding process.*

From a process standpoint, a critical issue was encountered related to the adhesion of SU- 8 to the metallic surfaces of the pre-alignment fixtures and wafer supports. To mitigate this phenomenon, aluminum sheets were initially evaluated as an interfacial material during the early stages of process development; however, this solution proved insufficiently effective in preventing the undesired adhesion of the photoresist. The issue was ultimately resolved by replacing the aluminum sheets with Kapton films and implementing a sandwich configuration, which eliminated parasitic adhesion effects and preserved the integrity of the resist during the pre-alignment and bonding operations.

In parallel with the optimization of the bonding process, other formulations of the SU-8 family were also evaluated. In particular, SU-8 2100 required temperatures between (180 and 215) °C and applied forces ranging from (800 to 4000) N, confirming the greater processability of SU-8 100.

Finally, with the aim of improving process scalability, a dedicated fixture was introduced (Figure 2.23) for the simultaneous pre-alignment of up to four samples per cycle. The system demonstrated good bonding reproducibility across all processed devices (Table 2.6).

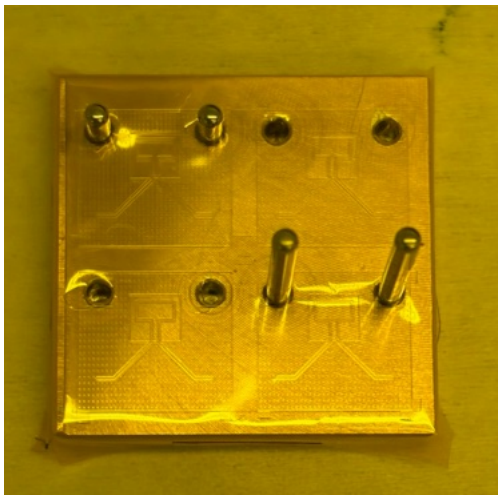

*Figure 2.23 Custom pre-alignment support designed for processing four devices per cycle.*

## 2.6 Experimental instrumentation and measurement setup

During the various stages of microfluidic device fabrication, periodic inspections were required to verify the correct realization of the structures and to monitor the effects of process parameters on the materials employed. For this purpose, a digital optical microscope and a profilometer were used, providing complementary information in the form of both qualitative observations and quantitative dimensional measurements.

The microscope was employed to inspect the fabricated structures, identify defects and imperfections, and verify alignment and bonding operations. The profilometer was used for the geometric characterization of the samples, enabling the measurement of film thicknesses, channel heights, and surface profiles. The combined use of these instruments allowed optimization of the fabrication process and validation of the characteristics of the manufactured devices.

### 2.6.1 Digital optical microscope

The Olympus DSX1000 digital microscope (Figure 2.24) [23] was systematically employed for sample inspection throughout the different stages of the microfabrication process, particularly after exposure, development, pre-alignment, and bonding. The system, equipped with both panoramic long-working-distance objective (1×) and high-resolution objectives (20× and 50×), enables the acquisition of high-detail images, 3D reconstructions, and direct geometric measurements.

*Figure 2.24 Olympus DSX1000 digital microscope.*

First, microscopic inspection represented a fundamental diagnostic tool for evaluating the quality of the thermocompression bonding process. The systematic analysis of the contact areas and defects observed after each experimental trial enabled continuous monitoring of interfacial bond stability and allowed the obtained results to be directly correlated with the applied process parameters. The collected evidence guided the planning of subsequent experiments and contributed to the identification of the most suitable operating window in terms of temperature, time, and pressure. In parallel, the observation of deformation, cracking, and microchannel collapse phenomena provided valuable insights for layout optimization, enabling the device geometry to be progressively adapted according to the actual structural responses observed experimentally (Figure 2.25).

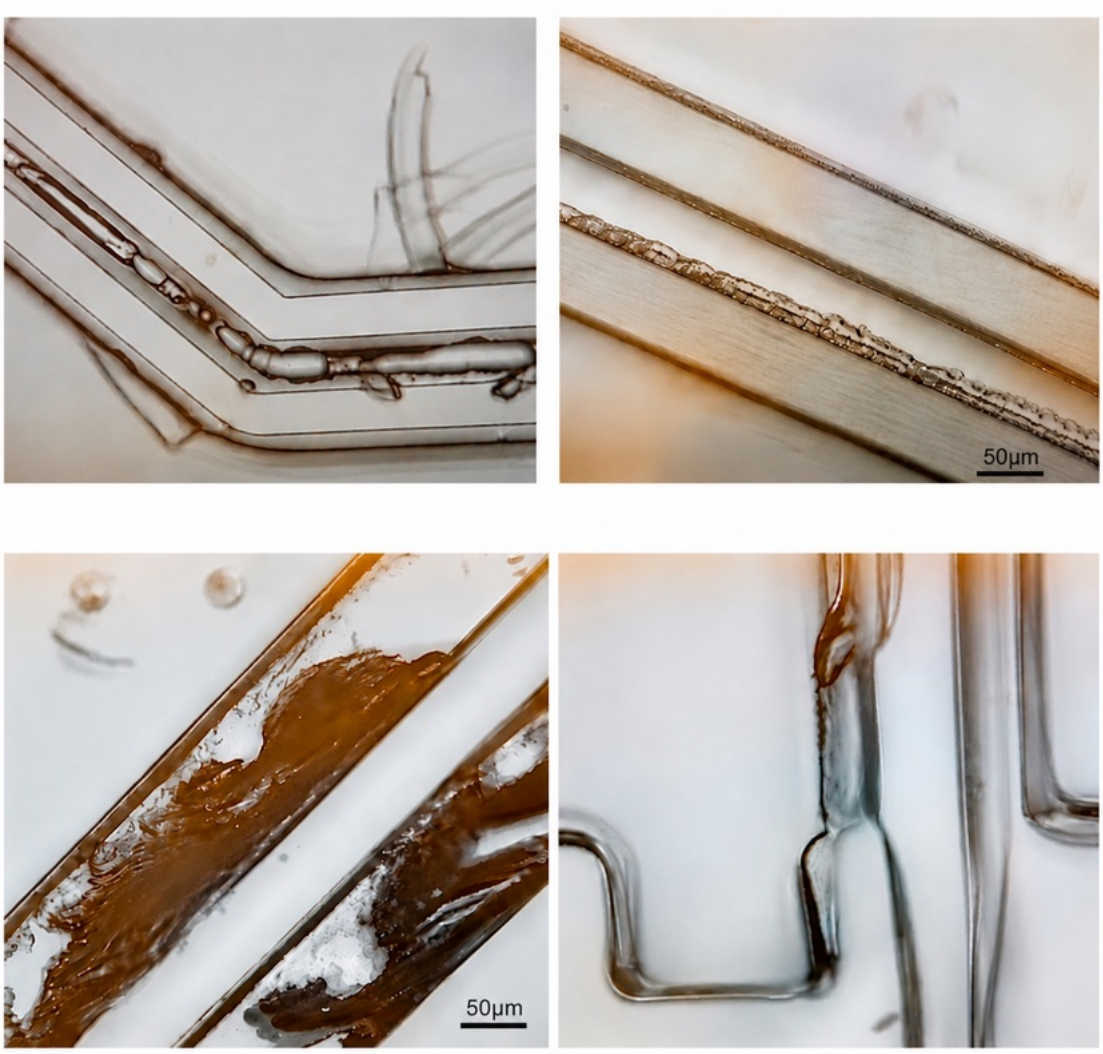


*Figure 2.25 Cracking and collapse of the microchannel walls following excessive thermomechanical loading.*

Post development inspection enabled the evaluation of the chemical process quality and the identification of possible fabrication defects. As shown in Figure 2.26, the analysis made it possible to distinguish underdevelopment conditions, characterized by the presence of unexposed photoresist residues within the microchannels, from overdevelopment conditions, associated with edge erosion phenomena and localized detachment of the structures from the substrate.

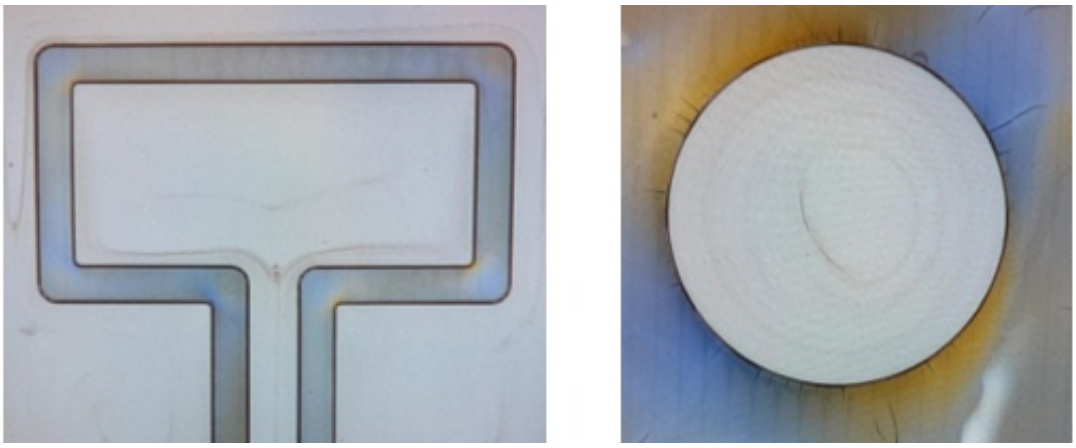

*Figure 2.26 Underdevelopment defects.*

Microscopic monitoring also highlighted the greater sensitivity of SU-8 100 to thermomechanical stresses compared with SU-8 2100, enabling the identification of cracking phenomena. Furthermore, this optical analysis allowed the determination of the optimal exposure dose required to minimize crack formation (Figure 2.27).

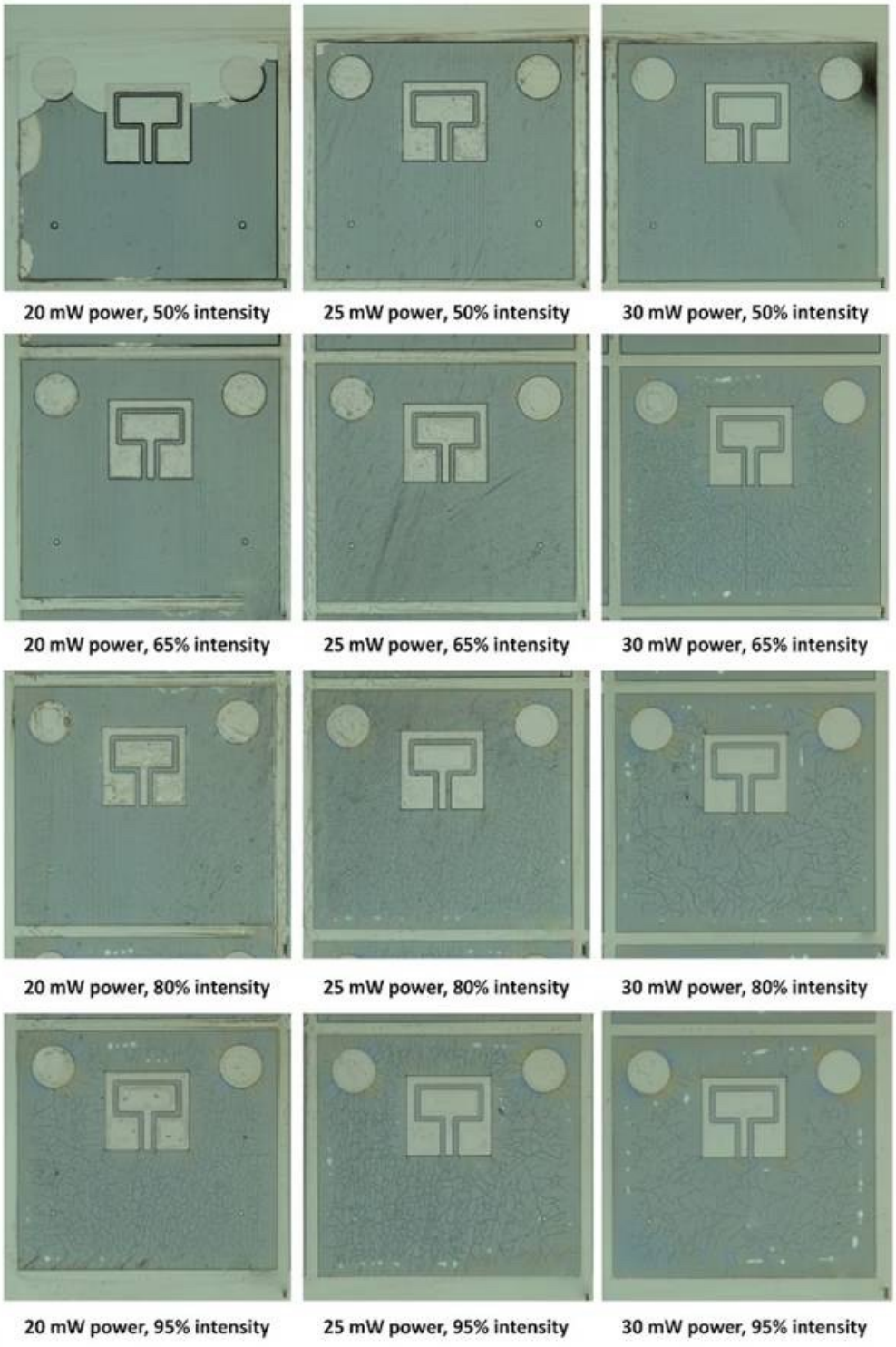


*Figure 2.27 Dose test performed at different laser power and exposure settings.*

In the subsequent stages, the microscope was used to verify the pre-alignment procedure performed at 120 °C. In particular, it enabled the inspection of the alignment between the inlet and outlet holes patterned in the covers and the microchannels fabricated in the bases, as well as the evaluation of the effectiveness of the adopted pre-alignment conditions in terms of temperature and holding time (Figure 2.28).

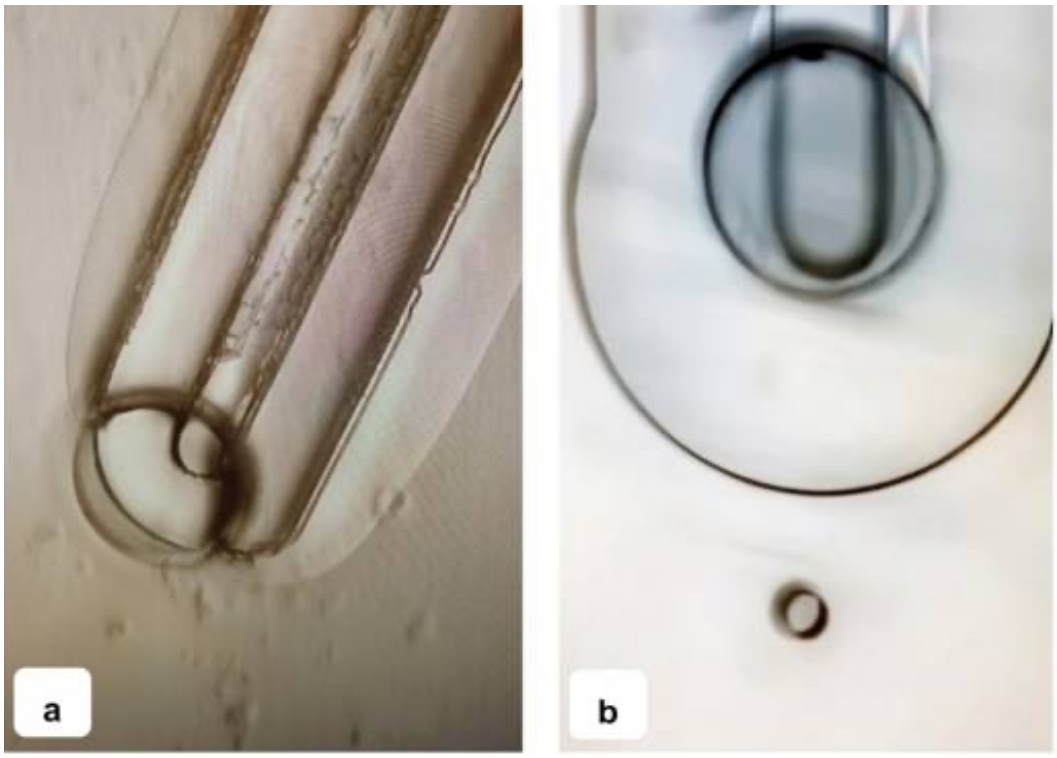


*Figure 2.28 Alignment verification between cover openings and microchannels: (a) incorrect alignment; (b) correct alignment.*

Finally, isopropanol flow tests observed at low magnification (Figure 2.29) enabled verification of microchannel continuity, the absence of obstructions, and the quality of the sealing, providing an initial functional validation of the device.

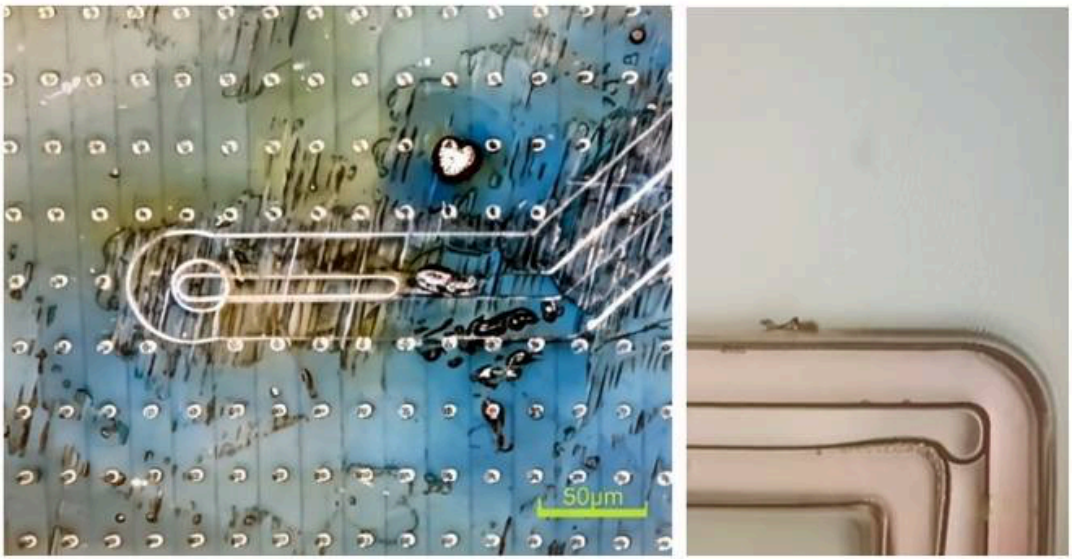


*Figure 2.29 Preliminary isopropanol flushing test showing fluid propagation in microchannels for verification of flow continuity and sealing quality.*

### 2.6.2 Profilometry for topographical and dimensional characterization of microchannels

Contact profilometry, performed using the KLA P-17 stylus system (Figure 2.30) [22], provided quantitative and 3D surface characterization, complementing the qualitative information obtained through optical microscopy. The instrument, equipped with a 2 µm diamond stylus, enables step height measurements with nanometric resolution, making it particularly suitable for monitoring and metrological validation of the various stages of the microfabrication process.

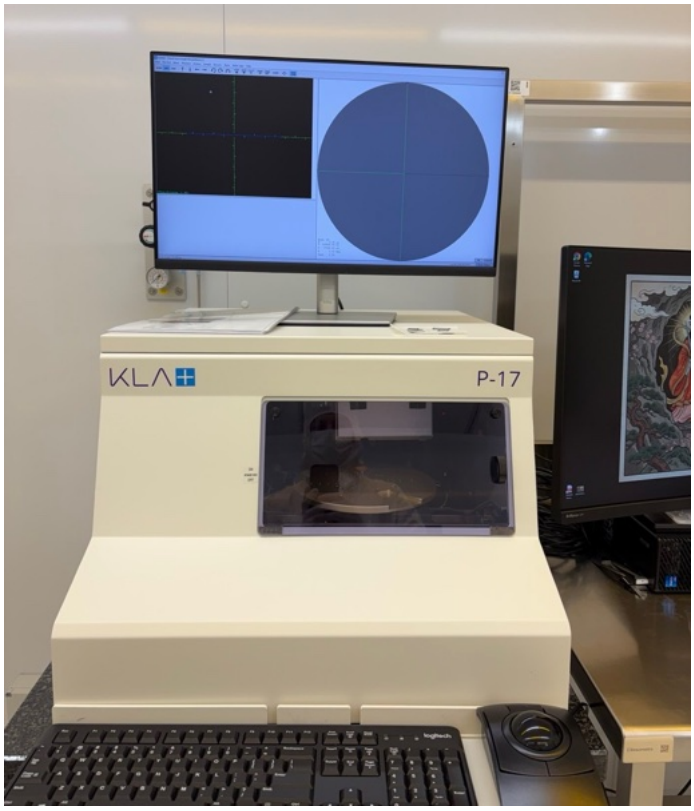


*Figure 2.30 Contact profilometer (KLA P-17) used for quantitative topographical and dimensional characterization of microfabricated structures.*

In a first stage, profilometry was used to characterize the thickness of the SU-8 layers obtained by spin coating. The measurements, performed with respect to the profilometer reference plane, allowed the thicknesses of the bases and covers to be determined and

verified against the design specifications. The main results of the profilometric scans are presented in Figures 2.31 and 2.32.

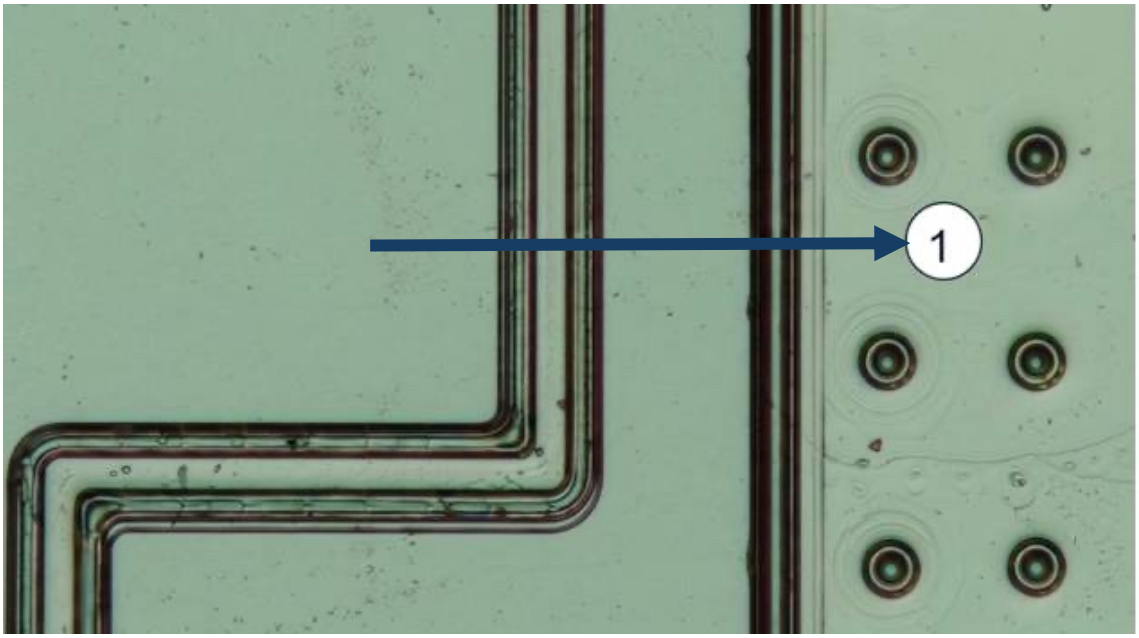


*Figure 2.31 Profilometric scan of the Ω-shaped region showing the reference plane and the height of the microchannels. Arrow (1) denotes the scan direction.*

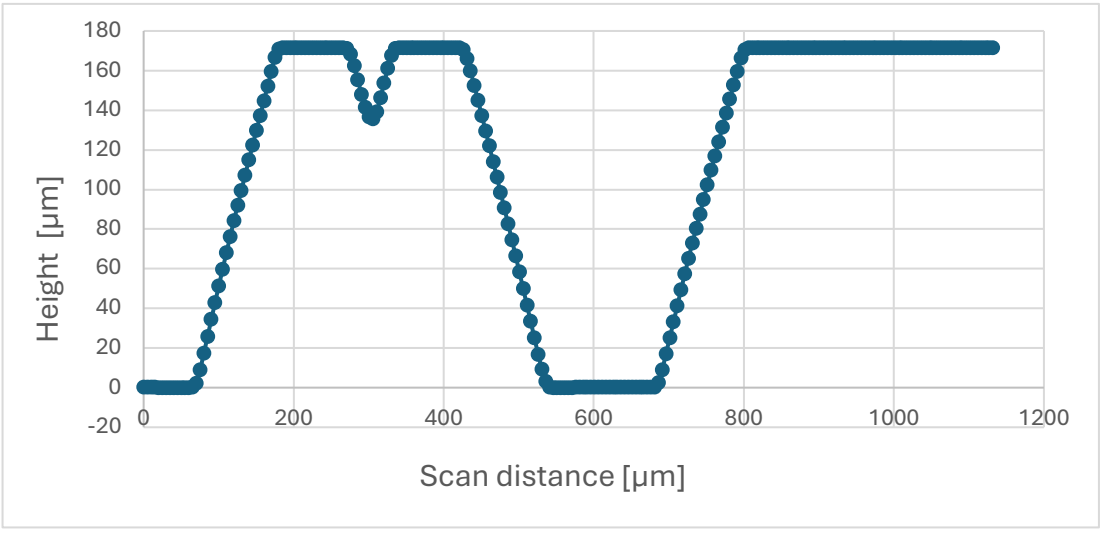


*Figure 2.32 Profilometric profile used for the dimensional characterization of the fabricated structures.*

Figures 2.33 and 2.34 show the detailed profilometric measurement of the microchannel layer, used to determine its characteristic height.

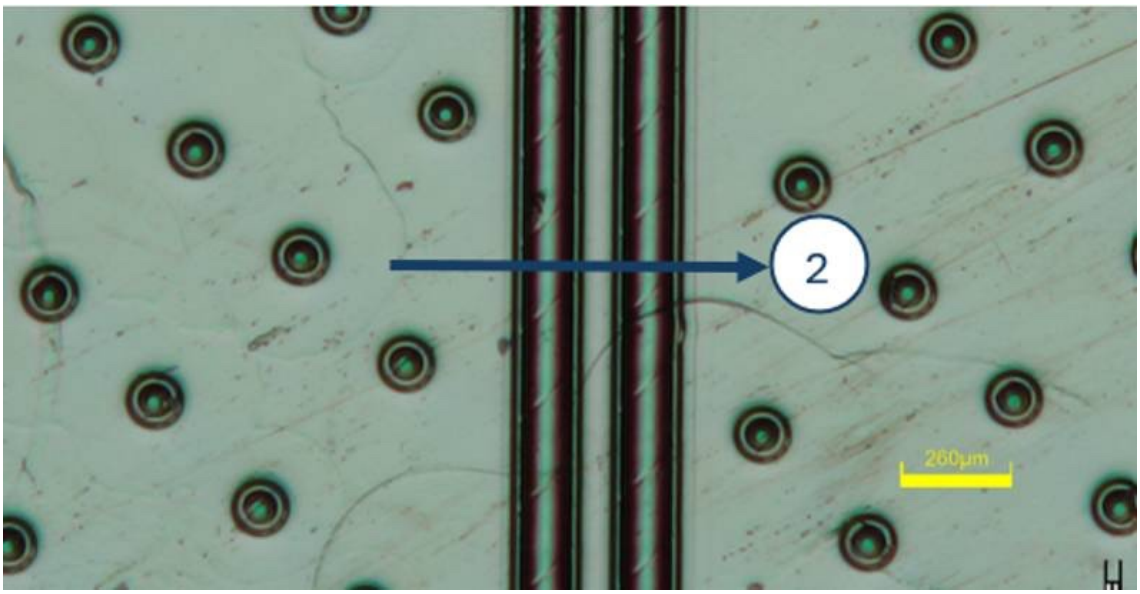


*Figure 2.33 Profilometric scan of the microchannel region. Arrow (2) denotes the scan direction.*

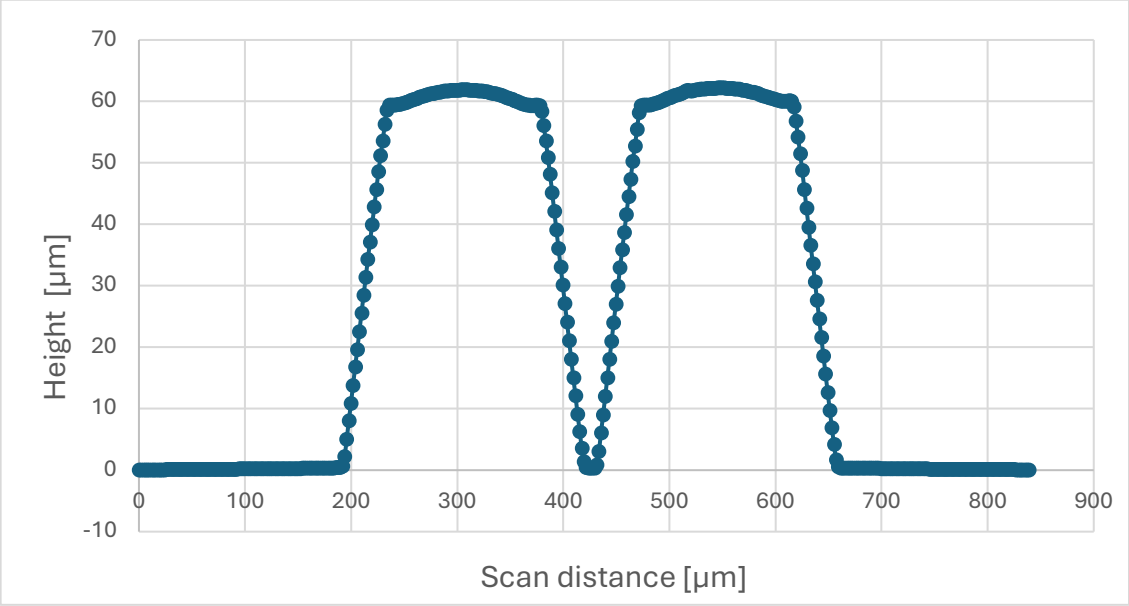


*Figure 2.34 Height profile of the microchannel layer obtained from profilometric measurements.*

Figures 2.35 and 2.36 show the profilometric measurement of the cap layer, used to determine its thickness.

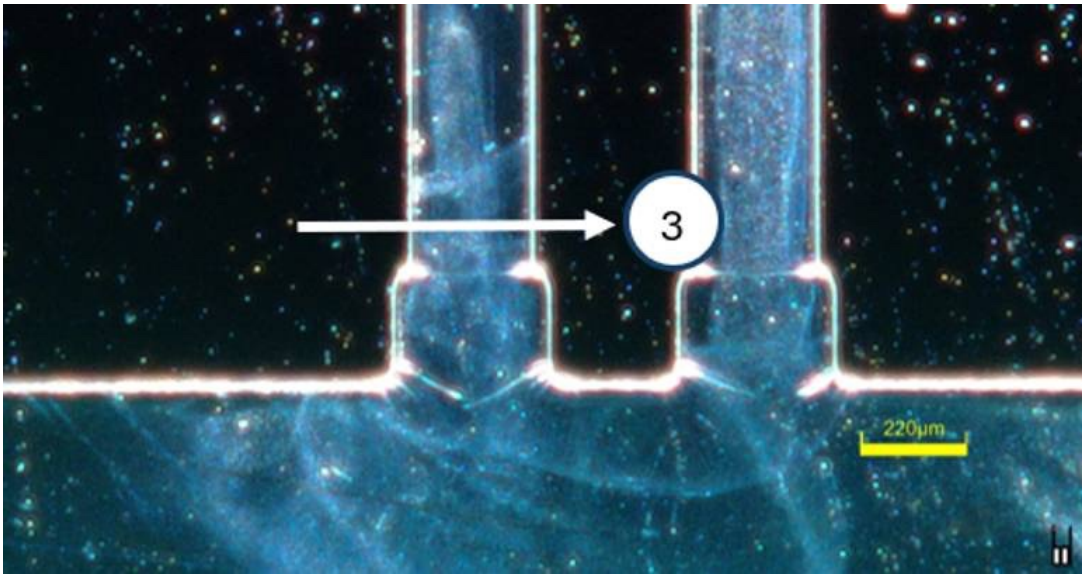


*Figure 2.35 Profilometric scan of the top layer. Arrow (3) denotes the scan direction.*

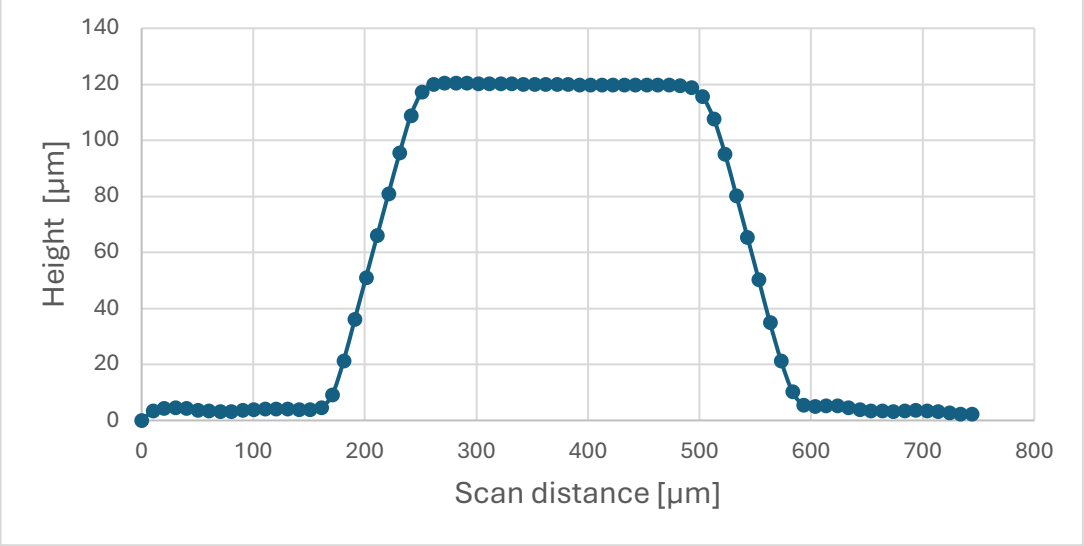


*Figure 2.36 Thickness profile of the top layer obtained from profilometric measurements.*

The set of profilometric measurements enabled a complete dimensional characterization of the fabricated structures. The results confirmed the correct deposition of the SU-8 layers and the good reproducibility of the fabrication process, with thickness and microchannel geometry values in agreement with the design specifications.

# 3 Results and discussion

The functional validation of the Coriolis microsensors fabricated in SU-8 100 required an extensive experimental campaign aimed at evaluating both the fluidic performance and the dynamic response of the devices. After device fabrication and hermetic sealing of the microchannels, the testing activity was focused on assessing the sensor behavior under real operating conditions. The analysis of the results is divided into two sequential macro-phases: microfluidic characterization and dynamic characterization via piezoelectric actuation. The microfluidic tests enabled the evaluation of the effectiveness of the polymeric bond by measuring the hydraulic resistance under increasing pressure gradients and determining the maximum flow rates sustained before interface failure or delamination. Subsequently, the dynamic characterization of the microchannel was carried out driving it at its natural resonance frequency using an external piezoelectric transducer. This phase allowed the analysis of the vibrational response of the structure, determining its damping factors under different operating conditions and with various fluids inside the microchannels. The experimental data collected during the dynamic characterization were subsequently used to develop a semi-empirical calibration model relating the resonance frequency shift to the density of the confined fluid. The model was obtained through polynomial regression of the experimental measurements and was then experimentally validated using independent reference fluids. In addition, an uncertainty analysis was performed to assess the overall reliability and predictive capability of the proposed density estimation methodology. The integration of these results provides a comprehensive quantitative framework, useful for correlating fabrication parameters with geometric stability and dynamic performance of the microsensor.

## 3.1 Microfluidic characterization and hydraulic sealing assessment

The functional validation of the Coriolis microsensors included, as a first experimental phase, the fluidic characterization and the assessment of the hydraulic sealing of the microchannels. The primary objective of the tests was to determine the maximum pressure sustained by the homogeneous SU-8 100 bond, while also quantifying the system

performance at different flow regimes and identifying the experimental relationship between pressure and flow rate.

The experimental setup for the microfluidic characterization (Figure 3.1) is based on a Fluigent LineUp platform [24], equipped with a Flow EZ module for pressure and flow control and an adapter module for managing different pressure ranges during the experiments.


*Figure 3.1 Fluigent LineUp microfluidic control system used for pressure-driven flow characterization.*

The microsensor was housed in a custom mechanical interface for structural support and fluidic connection, designed *ad hoc* and modeled in SolidWorks (Figure 3.2). The support was developed through an iterative structural optimization process aimed at improving the geometric fit with the device and increasing the overall stability of the assembly. The successive design iterations led to a final configuration characterized by improved microsensor stability and more reliable fluidic connections for interfacing with the flow generation system.

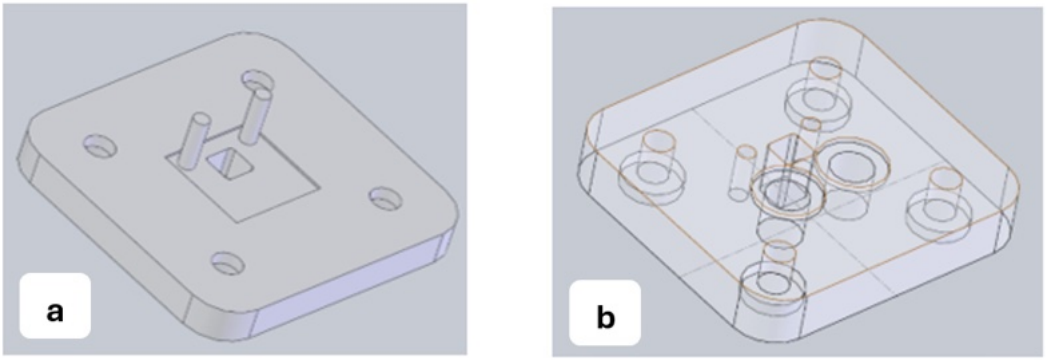


*Figure 3.2 Components of the optimized support for microsensor integration: (a) base; (b) cover.*

Visual inspection and real-time monitoring of the fluid within the Ω-shaped channels were carried out using a Leica DVM2500 [36] digital microscope, which enabled the tracking of the continuity of the advancing flow front (Figure 3.3).

*Figure 3.3 Leica Microsystems digital microscope used for real-time optical inspection of fluid flow within the Ω-shaped microchannels.*

To enhance optical contrast and facilitate the detection of potential micro-leaks or delamination paths at the bonding interface, the tests were performed using water mixed with red food dye (Figure 3.4).

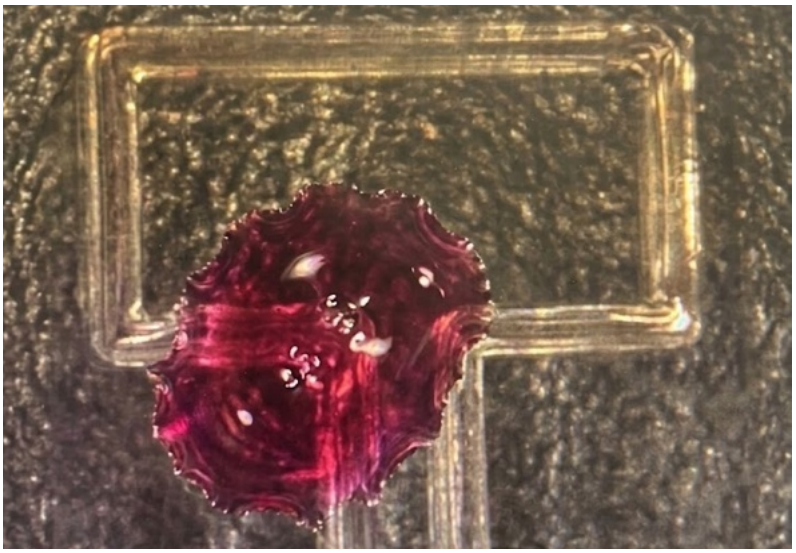

*Figure 3.4 Optical microscope image of the Ω-shaped microchannel showing fluid leakage caused by incomplete sealing of the bonded interface.*

The overall results confirmed the excellent structural effectiveness and high reliability of the thermocompression bonding process, optimized in Chapter 2. Nearly all tested systems exhibited an optimal hydraulic response, ensuring complete sealing of the bond without showing any delamination or leakage phenomena. The devices were able to sustain stable operating pressures up to approximately 1200 mbar, enabling flow rates of 200 µL/min. Although the pressure data recorded by the system are affected by minor localized pressure drops due to the geometry of the connectors in the support, the experimental analysis highlighted a clear and repeatable trend in the relationship between the applied pressure and the microsensor's fluidic response.

The quantitative data collected during the testing campaign, related to the main validated samples and their respective stable limit performances, are summarized in Tables 3.1, 3.2, and 3.3. The sample numbering refers to the different microsensor prototypes introduced in Chapter 2; the corresponding fabrication parameters are summarized in Table 2.6.

The pressure values highlighted in red indicate the onset of microchannel delamination and therefore identify the failure pressure of the corresponding device. All pressure values were measured using the Flow EZ module and are associated with a relative measurement uncertainty ($u_{r\,\%}$) of ± 0.367 %, according to the manufacturer's specifications.

*Table 3.1 Microfluidic flow tests performed on samples fabricated under different operating conditions.*

| ***Test*** | **1** | **2** | **3** | **4** | **5** | **6** | **7** | **8** | **9** | **10** | **11** |
|---|---|---|---|---|---|---|---|---|---|---|---|
| ***Q* [µL/min]** | **Pressure [mbar]** | | | | | | | | | | |
| ***1*** | 10 | 30 | 8 | 39 | 10 | 33 | 4 | 8 | 3 | 10 | 18 |
| ***10*** | 58 | 63 | 30 | 99 | | 52 | 49 | 50 | 52 | 52 | 55 |
| ***20*** | 119 | 108 | 58 | 166 | | 101 | 103 | 97 | 100 | 101 | 97 |
| ***30*** | 184 | 166 | | 240 | | 157 | 155 | 147 | 152 | 157 | 148 |
| ***40*** | 249 | 226 | | 319 | | 214 | 207 | 196 | 207 | 215 | 201 |
| ***50*** | 316 | 286 | | 397 | | 271 | 262 | | 263 | 274 | 253 |
| ***60*** | 379 | 346 | | 485 | | 330 | 320 | | 320 | 333 | 307 |
| ***70*** | 428 | 412 | | 570 | | 390 | 379 | | 379 | 392 | 365 |
| ***80*** | 500 | 481 | | 663 | | 450 | 435 | | 435 | 451 | 420 |
| ***90*** | | 582 | | 745 | | 513 | 494 | | 494 | 510 | 480 |
| ***100*** | | 650 | | 830 | | 574 | 554 | | 563 | 573 | 535 |
| ***110*** | | 720 | | | | 637 | 615 | | 624 | 637 | 591 |
| ***120*** | | 782 | | | | 707 | 676 | | 688 | 703 | 655 |
| ***130*** | | 820 | | | | 808 | 736 | | 750 | 768 | 720 |
| ***140*** | | 898 | | | | 878 | 797 | | 806 | 831 | 773 |
| ***150*** | | 968 | | | | 950 | 860 | | 870 | 899 | 863 |
| ***160*** | | 1040 | | | | 1000 | 924 | | 929 | 962 | 933 |
| ***170*** | | 1118 | | | | 1055 | 990 | | 1006 | 1028 | 995 |
| ***180*** | | 1131 | | | | 1129 | 1054 | | 1086 | 1100 | 1061 |
| ***185*** | | 1215 | | | | 1178 | 1085 | | 1120 | 1140 | 1091 |
| ***190*** | | 1247 | | | | 1219 | 1122 | | 1158 | 1159 | 1126 |
| ***193*** | | | | | | 1243 | 1145 | | 1178 | 1182 | 1140 |

| | | | | | |
|---|---|---|---|---|---|
| ***200*** | | 1193 | 1230 | 1228 | 1200 |
| ***201*** | | | | 1250 | |
| ***204*** | | 1249 | 1249 | | |
| ***207*** | | | | | 1251 |

Starting from sample 15, the flow rate increment step was modified from 10 µL/min to 20 µL/min in order to optimize the overall duration of the experimental campaign in regions characterized by lower variation in the pressure–flow response, while still maintaining adequate measurement resolution.

*Table 3.2 Flow characterization of devices fabricated at different applied bonding forces.*

| ***Test*** | ***12*** | ***13*** | ***14*** | ***15*** |
|---|---|---|---|---|
| ***Q* [µL/min]** | | **Pressure [mbar]** | | |
| ***1*** | 38 | 42 | 41 | 54 |
| ***10*** | 85 | 90 | 90 | |
| ***20*** | 133 | 141 | 140 | 153 |
| ***30*** | 180 | 191 | 191 | |
| ***40*** | 228 | 242 | 241 | 277 |
| ***50*** | 276 | 292 | 292 | |
| ***60*** | 327 | 338 | 342 | 381 |
| ***70*** | 375 | 392 | 392 | |
| ***80*** | 425 | 445 | 442 | |
| ***90*** | 478 | 499 | 494 | 555 |
| ***100*** | 529 | 555 | 539 | |
| ***110*** | 582 | 611 | 590 | |
| ***120*** | 637 | 666 | 641 | 701 |
| ***130*** | 690 | 723 | 695 | |
| ***140*** | 744 | 780 | 745 | 862 |
| ***150*** | 796 | 838 | 798 | |
| ***160*** | 854 | 896 | 848 | 917 |
| ***170*** | 910 | 954 | 900 | |
| ***180*** | 967 | - | 925 | 993 |

| | | | | |
|---|---|---|---|---|
| ***185*** | 1030 | 1016 | 952 | |
| ***190*** | - | | 970 | |
| ***193*** | - | 1074 | 1007 | 1155 |
| ***200*** | - | - | - | |
| ***204*** | 1080 | 1136 | - | |
| ***210*** | 1140 | 1200 | - | |
| ***220*** | 1200 | 1270 | - | |
| ***230*** | 1258 | - | - | |
| ***240*** | 1311 | - | - | |
| ***250*** | 1372 | - | - | |
| ***260*** | 1426 | - | - | |

*Table 3.3 Flow characterization of devices fabricated under different bonding force conditions.*

| ***Test*** | ***18*** | ***19*** | ***20*** | ***21*** |
|---|---|---|---|---|
| ***Q* [µL/min]** | | **Pressure [mbar]** | | |
| ***1*** | 20 | 54 | 12 | 13 |
| ***10*** | 57 | | | |
| ***20*** | 110 | 135 | 160 | 102 |
| ***30*** | | | | |
| ***40*** | 194 | 273 | 300 | 180 |
| ***50*** | | | | |
| ***60*** | 270 | 405 | 419 | 261 |
| ***70*** | | | | |
| ***80*** | 361 | 536 | 550 | 352 |
| ***90*** | | | | |
| ***100*** | 434 | 670 | | 441 |
| ***110*** | | | | |
| ***120*** | 508 | 802 | | 530 |
| ***130*** | | | | |
| ***140*** | 531 | 940 | | 615 |
| ***150*** | | | | |
| ***160*** | 628 | 1080 | | 702 |
| ***170*** | | | | |

| | | |
|---|---|---|
| ***180*** | 704 | 1225 |
| ***185*** | | |
| ***190*** | | |
| ***193*** | | |
| ***200*** | 810 | 1360 |
| ***204*** | | |
| ***210*** | | |
| ***220*** | 905 | 1509 |
| ***230*** | | |

The fluid dynamic behavior of the different devices and the corresponding performance comparison are reported in the pressure–flow rate curves shown in Figures 3.5, 3.6, and 3.7.

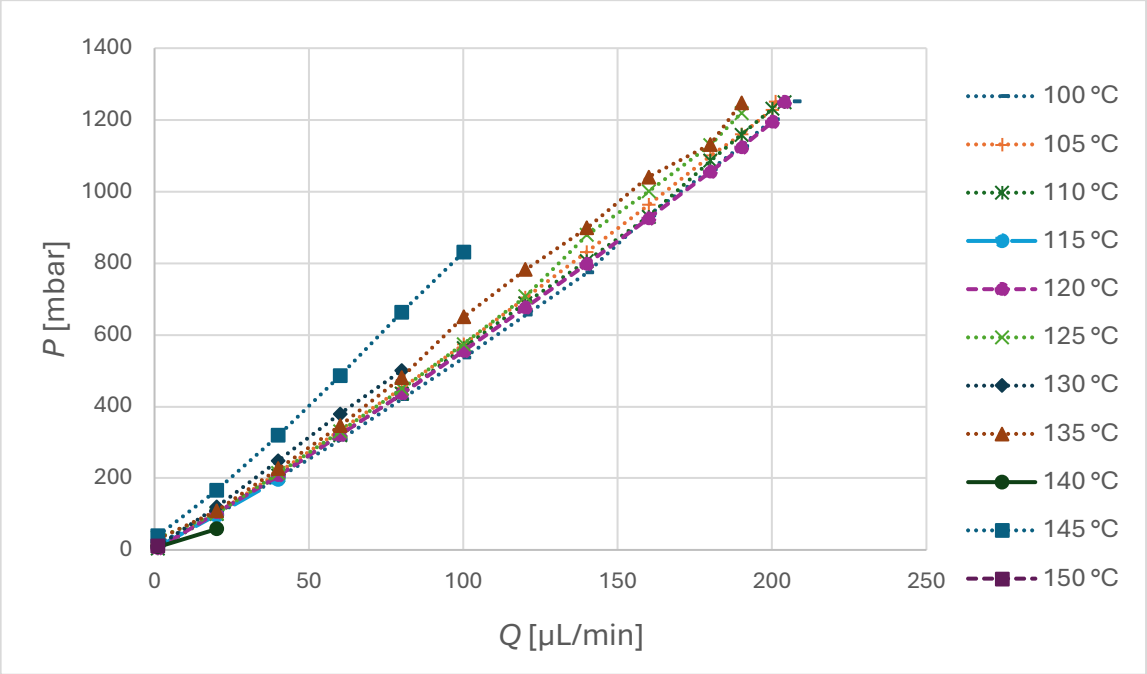


*Figure 3.5 Pressure versus flow rate behavior of devices fabricated at different bonding temperatures.*

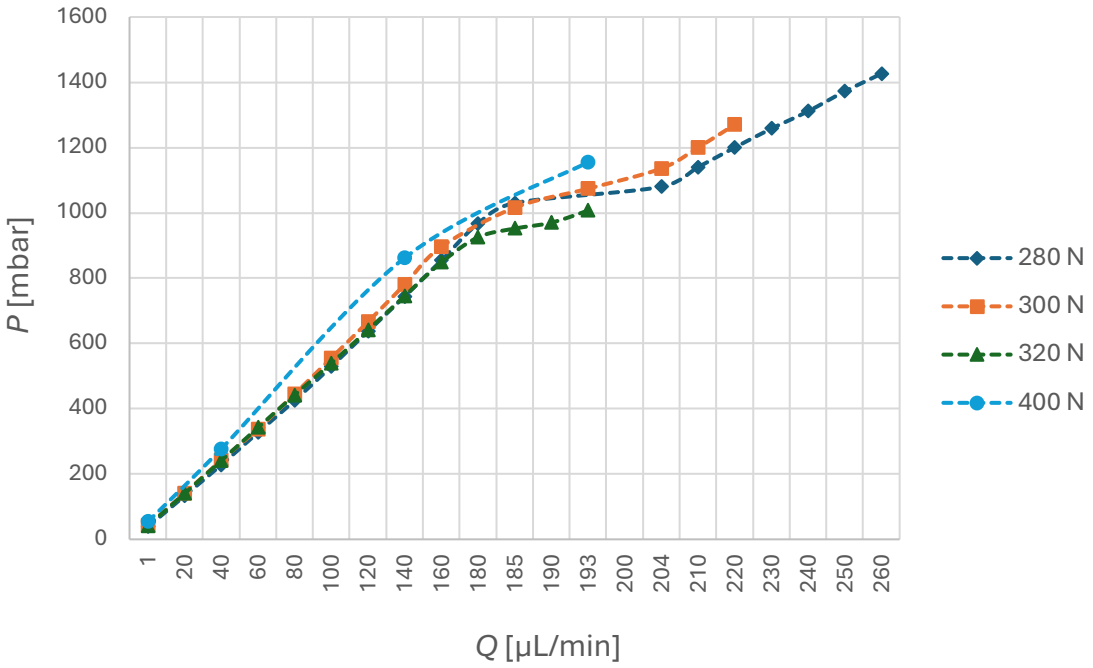


*Figure 3.6 Pressure versus flow rate behavior of devices fabricated under different applied bonding forces at 130 °C.*

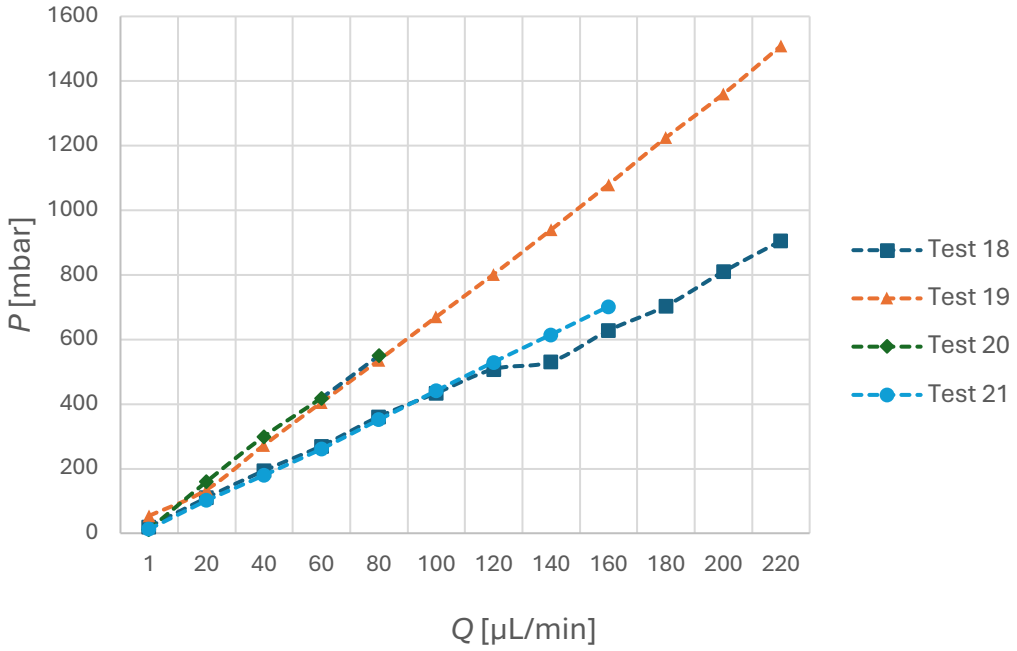


*Figure 3.7 Pressure versus flow rate behavior of devices fabricated in batch under varying bonding temperatures and forces.*

From the analysis of the curves, it emerges that the samples bonded at lower temperatures, while still within the optimal operating window, require lower inlet pressures for the same delivered flow rate. At the same time, these devices are able to reach higher maximum flow rates before the flow system operating limits are reached.

This behavior can be attributed to better preservation of the microchannel geometry during the bonding process. In fact, lower bonding temperatures reduce thermomechanical deformation, allowing the channels to maintain a more uniform cross-sectional profile closer to the designed geometry. The reduction of local constrictions and geometric variations along the fluidic path leads to lower pressure losses and higher hydraulic conductance, resulting in the improved experimental performance observed.

## 3.2 Dynamic characterization via piezoelectric actuation

The experimental characterization of the Coriolis microsensor was carried out to evaluate its performance as a density meter sensor and to develop a calibration curve capable of correlating the dynamic response of the device with the density of the fluid confined within the microchannel.

As described in Chapter 1, the presence of a fluid inside the vibrating microchannel alters the effective mass of the oscillating system, resulting in a shift of the microsensor resonance frequency. As the fluid density increases, the overall mass of the system increases accordingly, leading to a progressive decrease in the resonance frequency. This behavior constitutes the physical principle underlying the densimetric measurement approach adopted in the present work.

The dynamic properties and vibrational behavior of the Coriolis microsensors were experimentally characterized using a Micro System Analyzer LDV MSA-060 (Figure 3.8a) [26, 27], for optical measurements, while the Ω-shaped device was mechanically excited by coupling it to an external piezoelectric actuator (Figure 3.8b).

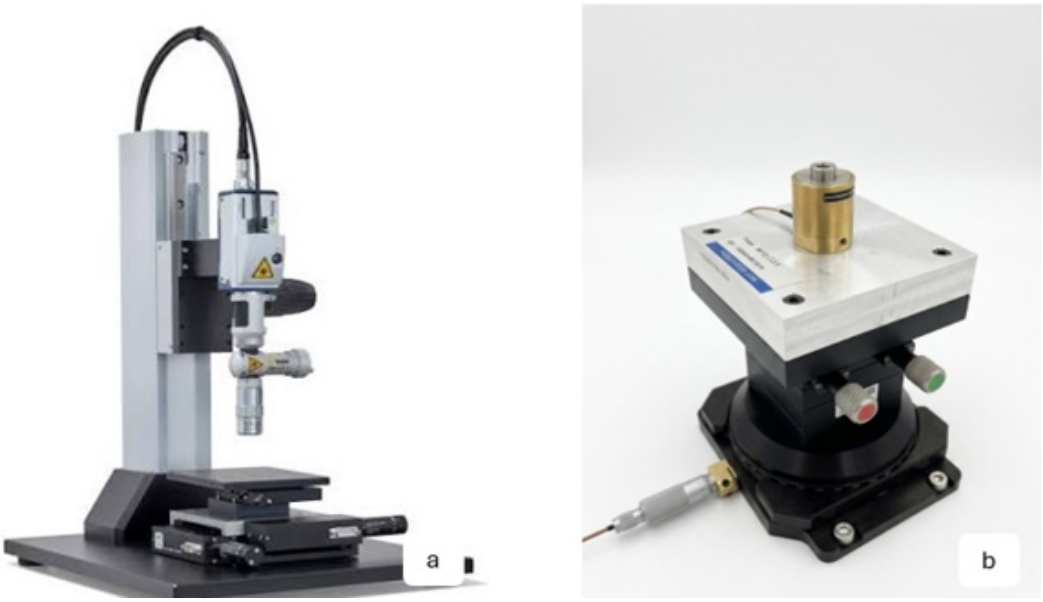


*Figure 3.8 Experimental setup for dynamic characterization of the Coriolis microsensor: (a) LDV MSA-060 Micro System Analyzer employed for non-contact optical vibration measurements; (b) piezoelectric actuation system used for mechanical excitation of the Ω-shaped microsensor.*

Finally, the frequency spectrum analysis and the identification of the resonance frequency were performed using an HP35670A Dynamic Signal Analyzer (Figure 3.9) [37].

*Figure 3.9 HP35670A Dynamic Signal Analyzer [37] used for resonance frequency measurements of the Coriolis microsensor.*

To enable the integration of the microsensor with the actuation system, the dedicated mechanical holder described in the previous section was modified to ensure full compatibility with the piezoelectric actuator and to provide efficient transmission of vibrational energy to the microsensor (Figure 3.10a, b).

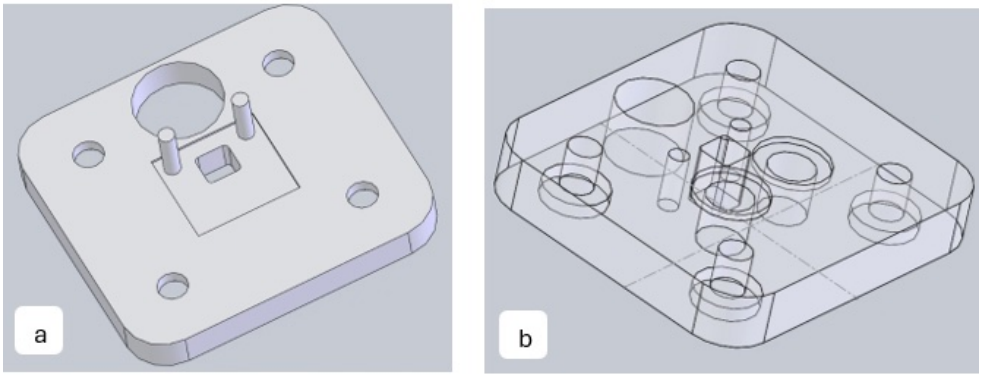


*Figure 3.10 Components of the custom support adapted for integration with the piezoelectric actuator: (a) base; (b) cover.*

Once the assembly was completed, the microfluidic connections were established using flexible tubing connected to a graduated syringe (Figure 3.11), allowing the controlled injection of fluids into the microchannel and their replacement during the different experimental tests.

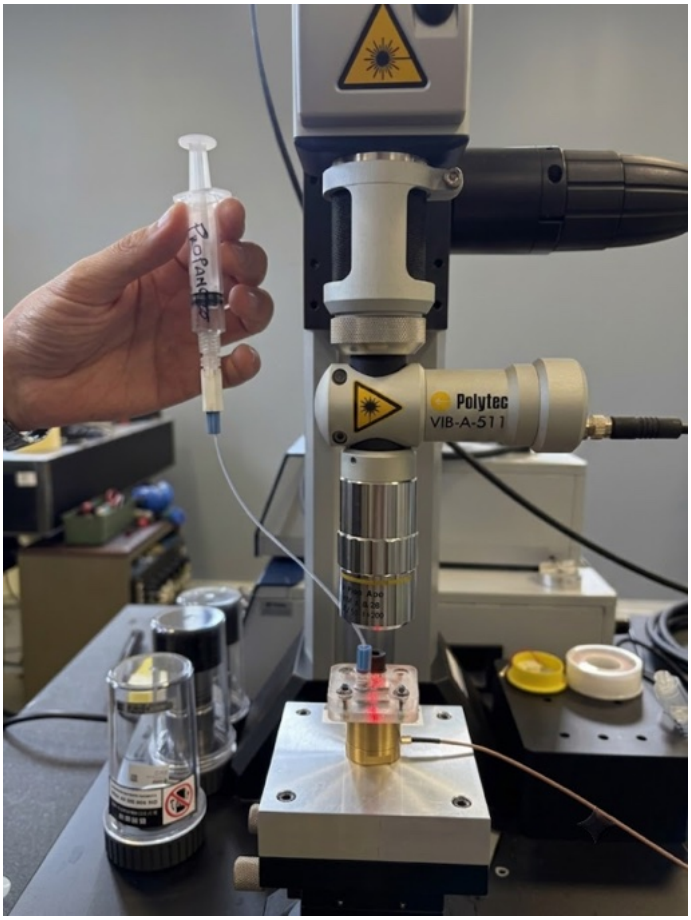


*Figure 3.11 Experimental fluid injection system used for filling the microsensor microchannel.*

The piezoelectric actuator was driven by an acoustic burst generated by a function generator Agilent 33250A. After identifying the fundamental resonance frequency of the microchannel, the excitation frequency was set close to this value in order to minimize the influence of possible harmonics introduced by the actuation chain. The actuator was excited with 1000-cycle bursts at 11 kHz, generated every 5 seconds. This operating configuration, kept constant throughout all measurements, provided a more stable

frequency response and a better-defined resonance peak, thereby enabling a more accurate determination of the characteristic resonance frequency.

The experimental campaign aimed at developing the calibration curve of the microsensor as a density meter was carried out by introducing into the microchannel a series of reference fluids with known densities spanning a wide density range. Air was used as the reference condition to define the zero of the measurement by assuming a resonance frequency shift equal to zero ($\Delta f = 0$). The subsequent experimental points were obtained using bidistilled water, 2-propanol, oxymethylene ethers (OME3 and OME4), and nonane. Oxymethylene ethers belong to a family of oxygenated synthetic compounds widely employed as reference fluids for the characterization of thermophysical properties owing to their high purity, chemical stability, and the availability of accurately certified density values. All experiments were performed under laboratory conditions at an ambient temperature of 23 °C and atmospheric pressure.

For each fluid, five independent measurements of the resonance frequency were performed while maintaining an unchanged experimental configuration in order to evaluate the repeatability of the measurement system and to quantify the variability associated with resonance frequency identification. The resonance frequency was determined using the dynamic signal analyzer by identifying the dominant peak in the frequency response spectrum. The expanded uncertainty associated with each frequency measurement, calculated with a coverage factor of ($k$ = 2), was ± 0.003 kHz and was obtained by combining the instrumental uncertainty of the LDV system with the spectral resolution of the signal analyzer.

The repeated measurements exhibited a natural dispersion of the acquired values, attributable both to the uncertainty associated with resonance peak identification and to the high sensitivity of the microsensor to small external perturbations, such as contaminants or particulate matter within the microchannel and the unavoidable fluctuations of the environmental conditions during testing. The average values obtained throughout the experimental campaign are summarized in Table 3.4, while the corresponding frequency response spectra are presented in Figure 3.12. All dynamic measurements were performed on the device bonded at 125 °C, 400 N, and 2 min, as these processing conditions provided the best structural integrity and enabled the microsensor to withstand the dynamic excitation without delamination or mechanical failure.

*Table 3.4 Resonance frequency measurements obtained from five consecutive acquisitions using 1000-cycle burst excitation for the reference fluids employed in the calibration procedure.*

| ***Sample*** | ***125 °C, 400 N, 2 min*** | | | | |
|---|---|---|---|---|---|
| | **Frequency [kHz]** | | | | |
| ***Air*** | 16.187 | 16.186 | 16.208 | 16.209 | 16.219 |
| ***2-propanol*** | 15.796 | 15.823 | 15.810 | 15.801 | 15.809 |
| ***OME 4*** | 15.708 | 15.692 | 15.681 | 15.702 | 15.682 |
| ***Bidistilled water*** | 15.724 | 15.725 | 15.724 | 15.726 | 15.724 |
| ***OME 3*** | 15.702 | 15.699 | 15.704 | 15.699 | 15.691 |
| ***Nonane*** | 15.840 | 15.856 | 15.849 | 15.847 | 15.823 |

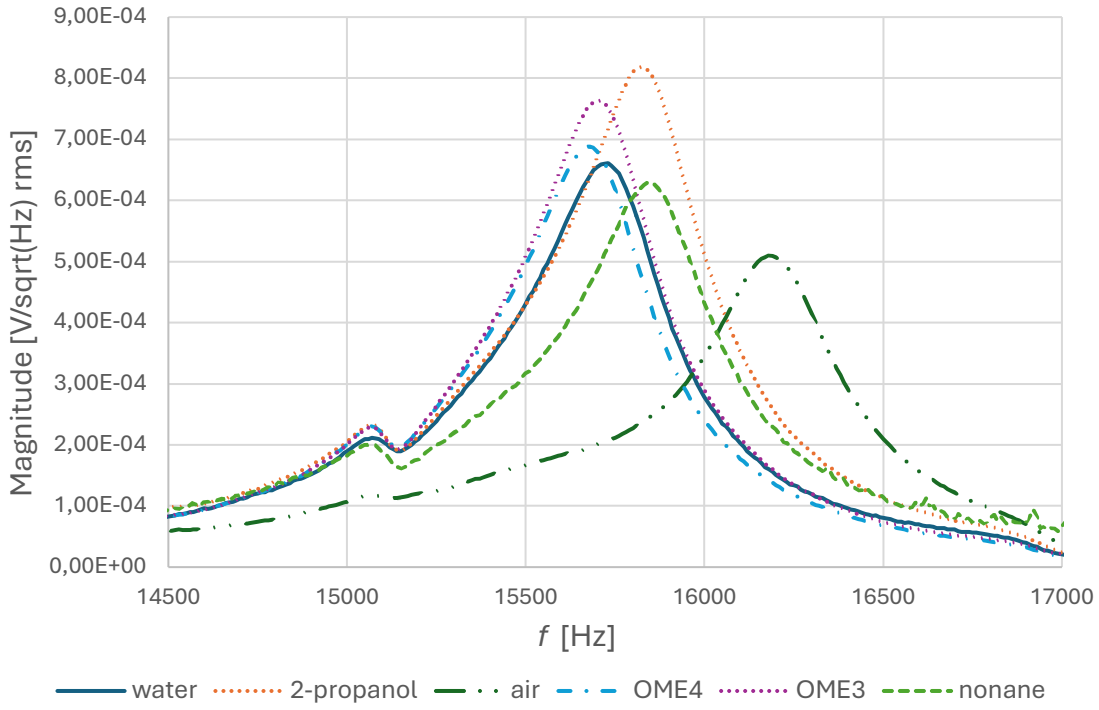


*Figure 3.12 Resonance magnitude spectra of the microsensor filled with air, water, 2-propanol, OME3, OME4, and nonane.*

As predicted by the operating principle of the Coriolis microsensor, the introduction of fluids with increasing density results in a progressive decrease in the resonance frequency. This behavior is attributed to the increase in the effective mass of the oscillating system, which leads to a reduction in the natural vibration frequency according to the theoretical relationship introduced in Chapter 1.

The acquired frequency response spectra exhibit a well-defined resonance peak for all the analyzed fluids, confirming the stability of the device's dynamic response and enabling the unambiguous identification of the resonance frequency used in the subsequent analyses.

Although the absolute resonance frequency is the quantity directly measured by the system, the resonance frequency shift defined by Equation 3.1 was adopted for the construction of the calibration curve:

$$\Delta f = f_{air} - f_{fluid} \tag{3.1}$$

where $f_{air}$ [kHz] is the resonance frequency measured with the microchannel filled with air, while $f_{fluid}$ [kHz] is the resonance frequency measured with the fluid under investigation. The use of $\Delta f$ eliminates the influence of the absolute resonance frequency of the individual device, making the calibration model less sensitive to geometric variations arising from the fabrication process and to differences introduced during sensor assembly.

The experimental campaign enabled the construction of a comprehensive dataset for the densimetric characterization of the microsensor. Table 3.5 summarizes, for each analyzed fluid, the mean resonance frequency ($\bar{f}$), the corresponding standard deviation ($\sigma$), the standard error of the mean (SEM), the percentage standard error of the mean (SEM %) and $\Delta f$ calculated with respect to the air reference.

*Table 3.5 Comparative analysis of resonance frequencies and spectral shift stability.*

| ***Fluid*** | $\rho_{meas}$ **[g/cm³]** | $\bar{f}$ **[kHz]** | $\Delta f$ **[kHz]** | $\sigma$ **[kHz]** | ***SEM* [kHz]** | ***SEM* %** |
|---|---|---|---|---|---|---|
| ***Air*** | 0.001 ± 0.002 | 16.1991 | - | 0.012 | 0.0053 | 0.0327 |
| ***2-propanol*** | 0.787 ± 0.002 | 15.8079 | 0.3913 | 0.010 | 0.0046 | 0.0291 |
| ***OME4*** | 1.070 ± 0.002 | 15.6930 | 0.5061 | 0.012 | 0.0053 | 0.0340 |
| ***Bidistilled water*** | 0.998 ± 0.002 | 15.7246 | 0.4745 | 0.001 | 0.0004 | 0.0027 |
| ***OME3*** | 1.027 ± 0.002 | 15.6991 | 0.5001 | 0.005 | 0.0022 | 0.0142 |
| ***Nonane*** | 0.718± 0.002 | 15.8430 | 0.3561 | 0.013 | 0.0056 | 0.0355 |

In addition, Table 3.5 reports the measured density values ($\rho_{meas}$), experimentally determined at a constant temperature of 23 °C in the INRiM laboratories using an Anton Paar DMA 5000M digital oscillating U-tube densimeter (Figure 3.13). The density values are reported together with the corresponding expanded uncertainty ($U_{\rho\,\%}$), calculated using a coverage factor of $k = 2$ corresponding to a 95% confidence level, in accordance with the international guidelines for the expression of measurement uncertainty (GUM).


*Figure 3.13 Anton Paar DMA 5000 M digital densimeter used for fluid density measurements based on the oscillating U-tube principle.*

## 3.3 Density estimation methodology

Starting from the experimental data collected during the characterization campaign, a semi-empirical methodology was developed to estimate fluid density from the resonance frequency shift of the microsensor. This section describes the development of the calibration model through polynomial regression of the experimental data, followed by its experimental validation using independent reference fluids. The uncertainty analysis associated with the proposed methodology is also presented to assess the overall reliability and accuracy of the density estimation.

### 3.3.1 Semi-empirical modeling and calibration of the microsensor

As discussed in Section 1.2 of Chapter 1, the operating principle of the microsensor is based on the variation of the resonance frequency of the polymeric microchannel resulting from changes in the mass of the confined fluid. The dynamic behavior of the system is described by Equation 1.4, which directly relates the resonance frequency $f_0$ to $k_D$ and the total system mass $m_{tot}$ (defined as the sum of the structural mass $m_{ch}$ and the fluid mass contribution given by $\rho \cdot V_{ch}$).

In principle, Equation 1.4 could be inverted to determine the density of an unknown fluid. However, its direct application presents significant practical limitations, since the parameters $k_D$, $m_{ch}$ and $V_{ch}$ cannot be regarded as known constants. Indeed, they depend on several factors, including the clamping conditions of the device, bonding process tolerances, and unavoidable geometric variations introduced during fabrication, which cannot be determined with sufficient accuracy under operating conditions. Moreover, the experimental characterization of these parameters would require dedicated microstructural measurement campaigns, which fall outside the scope and time constraints of the present work.

Starting from the original physical relationship, which links the density to the inverse square of the resonance frequency ($1/f^2$) and considering the limited operating range investigated, this dependence can be locally approximated by a second-order polynomial model. The mean values of the resonance frequency shift, calculated for each reference fluid with respect to the air-filled condition, were adopted as the independent variable.

The experimental data were then fitted using a least-squares second-order polynomial regression (Figure 3.14), yielding the following calibration model.

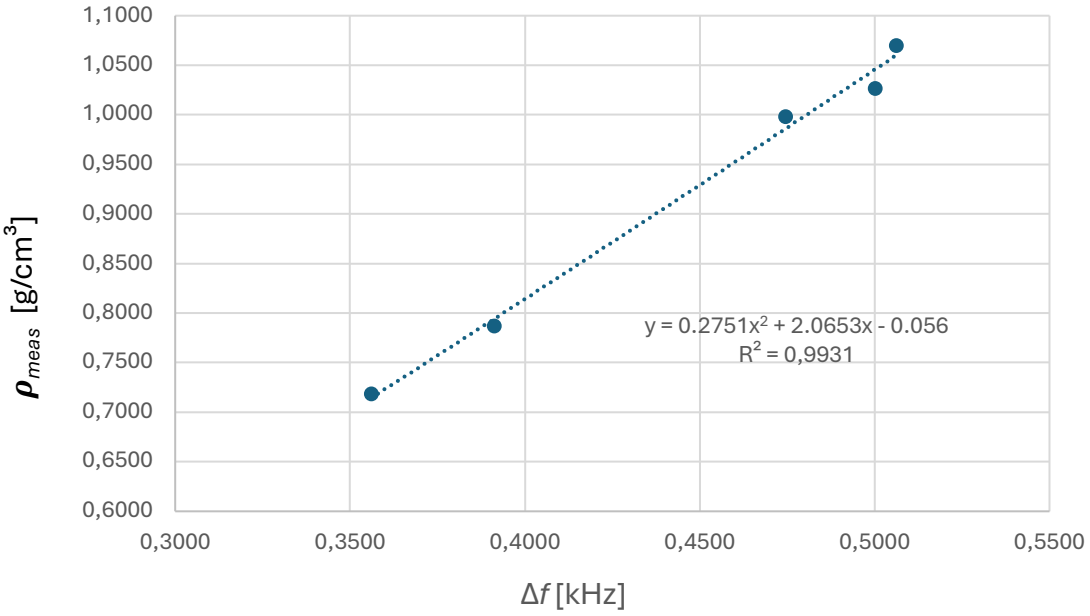


*Figure 3.14 Calibration curve showing the relationship between density and the frequency shift (Δf). Experimental data points and the second-order polynomial fit used for the semi-empirical model are reported, with a coefficient of determination $R^2$=0.9931.*

The model expresses the measured density ($\rho_{meas}$) for the different analyzed fluids as a function of the experimental resonance frequency ($\Delta f$) (Equation 3.2):

$$\rho_{meas} = a(\Delta f)^2 + b(\Delta f) + c \tag{3.2}$$

where $a$, $b$ and $c$ represent the calibration coefficients obtained through polynomial regression of the experimental data. From the interpolation of the experimental data of the reference fluids, the following calibration equation is obtained:

$$\rho_{meas} = 0.2751(\Delta f)^2 + 2.0653(\Delta f) - 0.056$$

A second-order polynomial was selected as the calibration model because it provides an accurate representation of the experimental data while minimizing the residuals. The quality of the fit was assessed through $R^2$, obtaining a value of 0.9931. This result indicates that the proposed model accurately captures the relationship between the resonance frequency shift and the fluid density within the investigated calibration range. However, $R^2$ alone does not constitute a validation of the model. Therefore, its predictive capability was subsequently assessed through an independent experimental validation using two reference fluids that were not included in the calibration dataset, as described in the following section.

### 3.3.2 Calibration curve uncertainty estimation

The validity of the model was initially quantified through a systematic residual analysis (Equation 3.3). For each reference fluid, the experimental value of $\Delta f$ was input into the calibration model in order to obtain the estimated density ($\rho_{est,i}$), subsequently computing the pointwise residual ($res_i$) as the difference with respect to the $\rho_{meas,i}$:

$$res_i = \rho_{meas,i} - \rho_{est,i} \tag{3.3}$$

The predictive capability of the system was then evaluated through the calculation of the root mean square error (RMSE*)* (Equation 3.4), derived from the squared residuals ($res_i^2$) according to:

$$\text{RMSE} = \sqrt{\frac{\sum_{i=1}^{n}(res_i)^2}{n}} \tag{3.4}$$

where *n* is the number of calibration data points used to construct the regression model.

The values obtained are reported in Table 3.6.

*Table 3.6 Comparison between $\rho_{meas}$ and $\rho_{est}$ densities for selected substances, including $res_i$ and $res_i^2$.*

| | $\boldsymbol{\rho_{meas}}$ [g/cm³] | $\boldsymbol{\rho_{est}}$ [g/cm³] | $\boldsymbol{res_i}$ [g/cm³] | $\boldsymbol{res_i^2}$ |
|---|---|---|---|---|
| ***2-propanol*** | 0.7870 | 0.7936 | -0.0066 | 4.34E-05 |
| ***OME4*** | 1.0700 | 1.0625 | 0.0075 | 1.11E-04 |
| ***Bidistilled water*** | 0.9982 | 0.9867 | 0.0115 | 1.32E-04 |
| ***OME3*** | 1.0266 | 1.0478 | -0.0212 | 3.55E-04 |
| ***Nonane*** | 0.7181 | 0.7147 | 0.0034 | 1.13E-05 |

The uncertainty associated with the calibration curve was subsequently expressed as the relative standard uncertainty ($u_c$) by normalizing the RMSE with respect to the mean measured density of the calibration dataset:

$$u_c = \frac{\text{RMSE}}{\rho_{mean}} \tag{3.5}$$

where $\rho_{mean}$ is the arithmetic mean of the measured densities of the calibration fluids.

Finally, the expanded percentage uncertainty ($U_{\rho\,\%}$) associated with the density measurements obtained from the calibration curve was determined by applying $k$ = 2, corresponding to a confidence level of approximately 95 % (Equation 3.6):

$$U_{\rho\,\%} = 100 \cdot u_c \cdot k \tag{3.6}$$

The calculated relative standard uncertainty was $u_c$ = 0.0127, corresponding to an expanded relative uncertainty of $U_{\rho\,\%}$ =2.54 %. This value was adopted as the expanded uncertainty associated with the density estimates obtained from the calibration curve and was subsequently used to evaluate the uncertainty of the density measurements reported throughout the validation procedure.

### 3.3.3 Experimental validation of the calibration model

To verify the predictive robustness of the semi-empirical model, an independent validation procedure was carried out using two reference fluids: APN26 and APN415. These compounds were not included in the initial regression phase, thus constituting an unbiased test set for evaluating the system accuracy. APN26 and APN415 are certified reference fluids widely used for the calibration and verification of density and viscosity measurement instruments in procedures compliant with ISO standards. Their well-characterized thermophysical properties make them particularly suitable for assessing the predictive capability of the proposed calibration model. The reference density values $\rho_{ref}$ were determined through specific thermal calibration curves obtained at a constant temperature of 23 °C. The linear relationships used to derive the nominal values are reported in Figures 3.15 and 3.16, which were obtained from the experimental data summarized in Table 3.7.

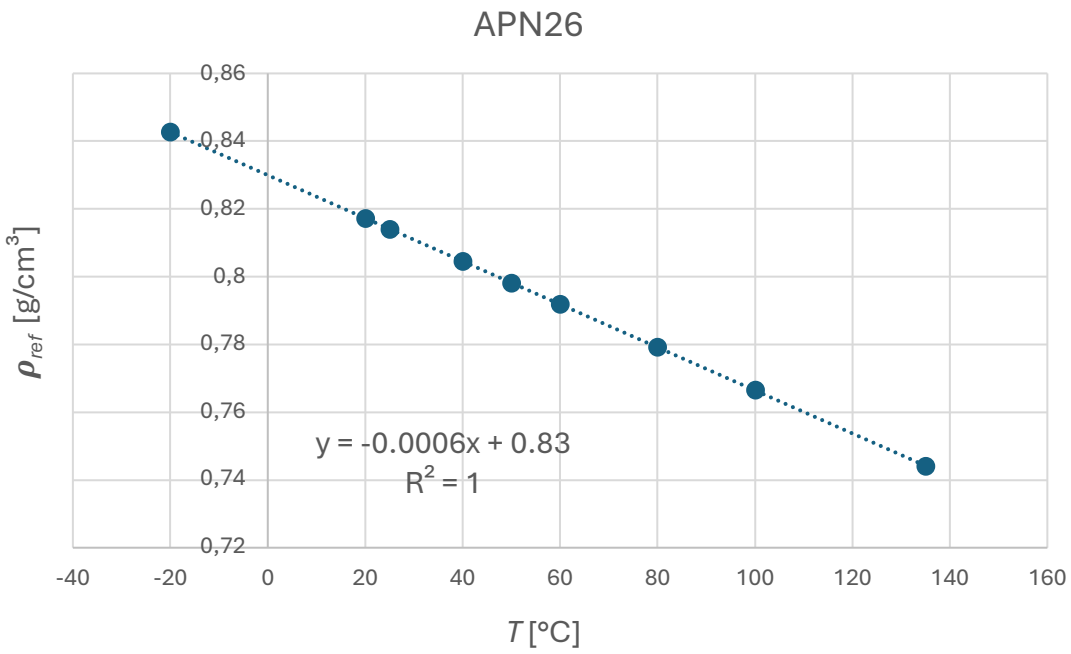


*Figure 3.15 Reference density calibration curve for APN26.*

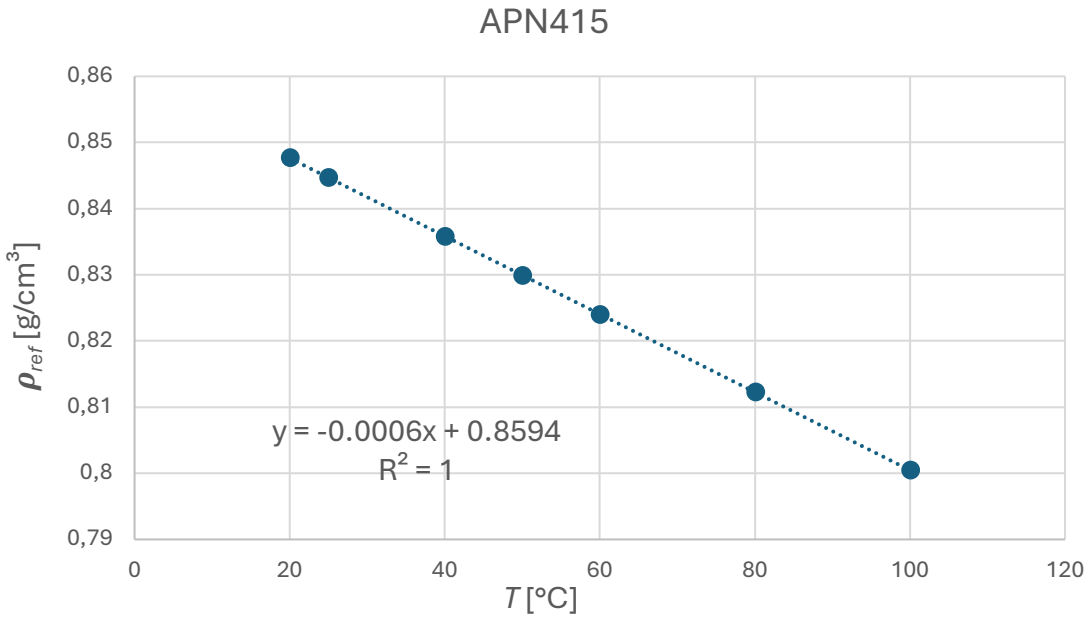


*Figure 3.16 Reference density calibration curve for APN415.*

*Table 3.7 Reference density values provided by the manufacturer at different temperatures.*

| | ***APN26*** | ***APN415*** |
|---|---|---|
| ***T* [°C]** | **$\rho_{ref}$ [g/cm³]** | |
| *-20* | 0.84276 | - |
| *20* | 0.81720 | 0.84769 |
| *25* | 0.81399 | 0.84470 |
| *40* | 0.80452 | 0.83580 |
| *50* | 0.79820 | 0.82992 |
| *60* | 0.79189 | 0.82401 |
| *80* | 0.77918 | 0.81226 |
| *100* | 0.76651 | 0.80051 |
| *135* | 0.74414 | - |

For each validation fluid, $\rho_{meas}$ was calculated by applying the polynomial calibration model to the experimentally measured $\Delta f$ values. The comparison between the measured densities and the corresponding reference values is reported in Table 3.8.

*Table 3.8 Density validation and error analysis for the investigated fluids.*

| ***Fluid*** | ***Δf*** | **$\rho_{ref}$ [g/cm³]** | **$\rho_{meas}$ [g/cm³]** | ***Err* [g/cm³]** | ***Err %* [%]** |
|---|---|---|---|---|---|
| ***APN26*** | 0.3981 | 0.8162 | 0.8091 | 0.0070 | -0.8667 |
| ***APN415*** | 0.4091 | 0.8456 | 0.8342 | 0.0114 | -1.3457 |

The absolute error Err [g/cm$^3$] was defined as the difference between the measured and reference density values, while the percentage relative error (Err %) was calculated according to Equation 3.7:

$$\text{Err } \% = 100 \cdot \frac{\rho_{meas} - \rho_{ref}}{\rho_{ref}} \tag{3.7}$$

In order to provide a graphical assessment of the predictive capability of the proposed calibration model, Figure 3.17 compares the regression curve with both the experimental data used for model calibration and the two independent validation fluids. Although the validation fluids were not included in the regression process, their experimental data closely follow the calibration trend, providing a first qualitative indication of the predictive capability of the proposed semi-empirical model over the investigated density range. A quantitative assessment of the model performance is subsequently provided through the uncertainty analysis presented in the following section.

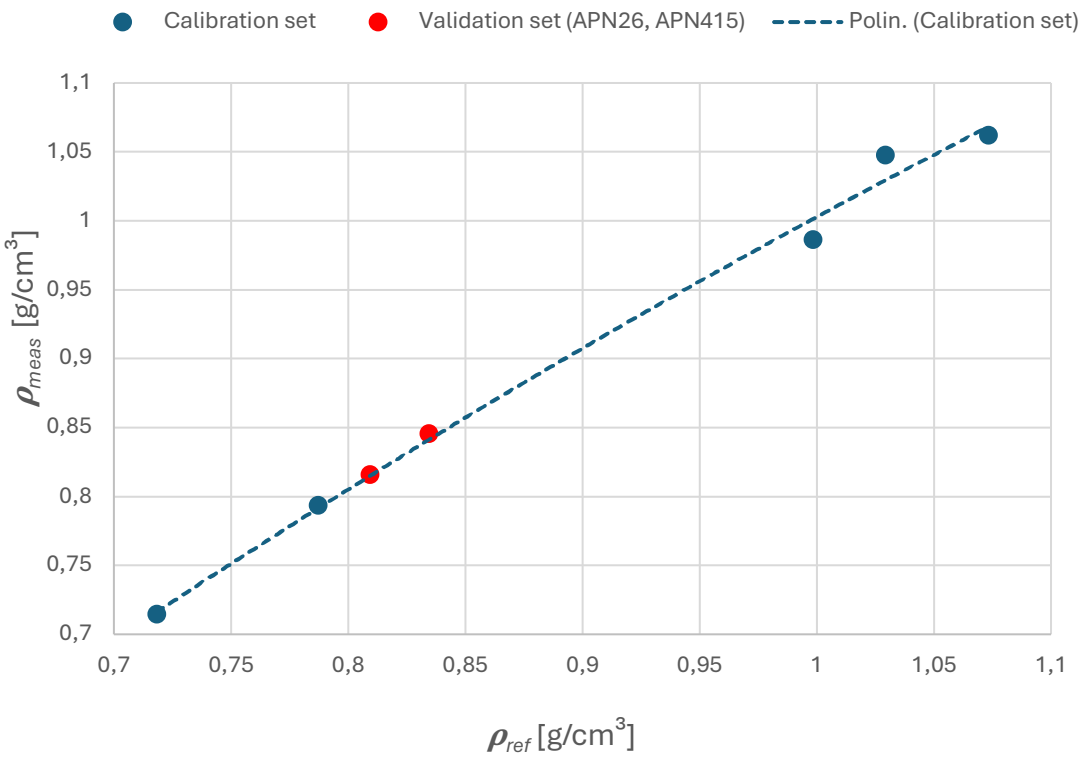


*Figure 3.17 Plot comparing $\rho_{meas}$ with $\rho_{ref}$. Calibration and validation fluids are identified using different markers.*

To further analyze the model accuracy within the investigated density range, the distribution of Err % as a function of the reference density was also examined. The graph reported in Figure 3.18 highlights the possible presence of systematic errors or a dependence of the model accuracy on the fluid density.

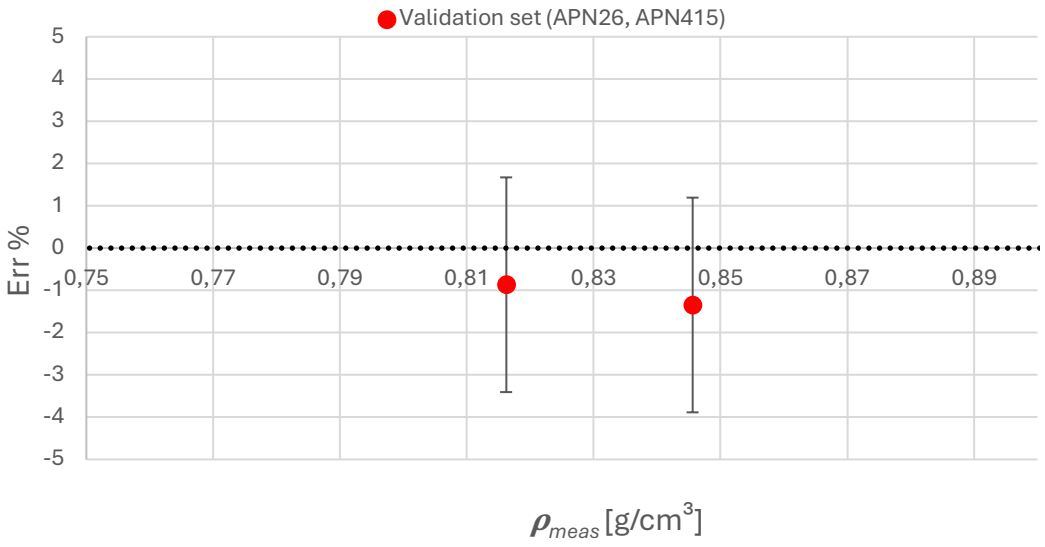


*Figure 3.18 Relative prediction error (%) of the measured density. The dashed line represents the zero-error condition and is used to assess the absence of systematic bias.*

The error bars shown in the graph represent the expanded uncertainty $U_{\rho\,\%}$, while the dashed line indicates the zero-error condition (corresponding to the reference density values), used as a reference for the identification of potential systematic biases. The results show a slight underestimation of the estimated values with respect to the reference densities. However, the observed deviations remain limited and are consistent with the uncertainty level of the system across the investigated density range.

The expanded uncertainty of ± 2.54 % is consistent with the nature of the system under investigation and with the initial development stage of the device, in which advanced optimization strategies such as vacuum encapsulation or on-chip readout integration have not been implemented yet. In this context, the achieved accuracy confirms the validity of the operating principle and the robustness of the adopted calibration approach, demonstrating a stable and reproducible behavior.

The experimental validation conducted on APN26 and APN415 demonstrated that the density values measured by using the calibration curve are in good agreement with the corresponding reference densities. This agreement confirms the predictive capability of the proposed model and validates its application for density estimation within the

investigated operating range. The calibration equation therefore represents the core of the Coriolis microsensor density estimation model and constitutes a reliable tool for density determination. Furthermore, the proposed methodology can be extended to additional fluids or mixtures, provided that an appropriate recalibration is performed for the corresponding density range and operating conditions.

# 4 Conclusions

This thesis successfully demonstrated the modeling, clean-room microfabrication, and experimental validation of a polymer-based micro-Coriolis sensor for mass flow rate and density measurements, entirely fabricated in SU-8 100 photoresist. The transition from conventional contact photolithography to direct laser writing represented a significant technological advancement, providing greater design flexibility and enabling the fabrication of high-aspect-ratio microchannels with nearly vertical sidewalls. Reliable hermetic sealing of the suspended microfluidic structure was achieved through thermocompression bonding between SU-8 layers, ensuring structural integrity and hydraulic sealing up to 1200 mbar.

From a metrological perspective, the dynamic characterization combined with laser Doppler vibrometry validated the operating principle of the device. The developed semi-empirical calibration model showed excellent agreement with the experimental data ($R^2 = 0.9931$) and provided reliable density estimation within the investigated operating range, with a combined expanded uncertainty of ± 2.54 % ($k = 2$). Considering that the proposed device represents an initial prototype and that advanced optimization strategies have not been implemented yet, these results confirm the suitability of polymer-based MEMS technology for fluid density characterization and provide a solid foundation for further developments.

From an industrial perspective, the adopted fabrication technology offers significant advantages in terms of scalability. Wafer-level fabrication enables the simultaneous production of multiple devices on a single silicon or glass substrate through batch processing. Compared with serial micromachining techniques, photolithography and wafer bonding allow the parallelization of deposition, exposure, and sealing steps, significantly reducing fabrication costs while ensuring high dimensional uniformity across devices, a fundamental requirement for large-scale manufacturing.

Although the current results successfully demonstrate the feasibility of the proposed sensor, further developments are required to achieve a fully autonomous metrological instrument. One of the main limitations is the aerodynamic viscous damping affecting the resonator. A key improvement will therefore be the implementation of vacuum encapsulation through wafer-level bonding, allowing the device to operate under low-vacuum conditions ($<10^{-1}$ mbar) and reducing intrinsic damping and measurement noise.

Future work will also focus on the direct integration of piezoelectric thin films, such as PZT, AlN, or PVDF, deposited by sputtering onto the microchannel surface using optimized low-temperature processes compatible with the polymer substrate. In addition, grayscale lithography could be adopted to directly define different microchannel heights within a single lithographic step, reducing the number of SU-8 exposure processes from three to two and further simplifying the fabrication process.

To eliminate the need for laboratory optical instrumentation, the sensor architecture will evolve toward an integrated on-chip readout based on differential capacitive structures or piezoresistive strain gauges positioned at locations of maximum torsional stress. Interfaced with an application-specific integrated circuit (ASIC), these transducers will enable continuous monitoring of the Coriolis-induced phase shift, providing simultaneous digital measurements of mass flow rate and fluid density.

Finally, the experimental validation will be extended to dynamic flow conditions over a wider flow-rate range (0.1–500 μL/min) and to a broader variety of fluids, including high-viscosity Newtonian liquids and biological samples. These investigations will enable the separate characterization of viscous damping and mass-loading effects and support the development of multivariable calibration algorithms capable of compensating for thermal drift and viscoelastic relaxation, ultimately improving measurement accuracy, long-term stability, and the applicability of the proposed sensor in biomedical and industrial fields.

# References


[1] R. Monge, J. Groenesteijn, D. Alveringh, R. J. Wiegerink, J. C. Lötters, and L. J. Fernandez, “SU-8 micro Coriolis mass flow sensor,” Sensors and Actuators B: Chemical, vol. 241, pp. 744-749, 2017.

[2] J. Haneveld, T. S. J. Lammerink, M. J. de Boer, R. G. P. Sanders, A. Mehendale, J. C. Lötters, et al., “Modeling, design, fabrication and characterization of a micro Coriolis mass flow sensor,” Journal of Micromechanics and Microengineering, 2010.

[3] R. Martinez-Duarte and M. Madou, “SU-8 photolithography and its impact on microfluidics,” in Microfluidics and Nanofluidics Handbook, 2011, ch. 38.

[4] A. C. de Oliveira, S. Pan, R. J. Wiegerink, and K. A. A. Makinwa, “A MEMS Coriolis-based mass-flow-to-digital converter for low flow rate sensing,” IEEE Journal of Solid-State Circuits, vol. 57, no. 12, pp. 3681-3692, 2022.

[5] J. Haneveld, T. S. J. Lammerink, M. Dijkstra, H. Droogendijk, M. J. de Boer, and R. J. Wiegerink, “Highly sensitive micro Coriolis mass flow sensor,” in Proc. IEEE 21st Int. Conf. Micro Electro Mechanical Systems (MEMS), 2008, pp. 920-923.

[6] R. Smith, D. R. Sparks, D. Riley, and N. Najafi, “A MEMS-based Coriolis mass flow sensor for industrial applications,” IEEE Transactions on Industrial Electronics, vol. 56, no. 4, pp. 1066-1071, 2009.

[7] D. Scaiola, S. Stassi, R. Calmo, D. Maillard, S. S. Varricchio, A. De Pastina, et al., “Fabrication of clamped-clamped beam resonators with embedded fluidic nanochannel,” Microelectronic Engineering, vol. 231, Art. no. 111395, 2020.

[8] Kayaku Advanced Materials, Inc., SU-8 Permanent Negative Epoxy Photoresist: Formulations 2-25 and 50-100, Technical Data Sheet, Rev. 9.3.20, 2020.

[9] Heidelberg Instruments Mikrotechnik GmbH, DWL 66+ Operator's Guide, Doc. No. HI-01837-UG03, Rev. 8, Heidelberg, Germany, May 2025.

[10] EV Group E. Thallner GmbH, EVG 510 Users Manual: Operator Manuals, EV Group, 2012.

[11] P. Enoksson, G. Stemme, and E. Stemme, “A silicon resonant sensor structure for Coriolis mass-flow measurements,” Journal of Microelectromechanical Systems, vol. 6, no. 2, pp. 119-125, 1997.

[12] Y. Zeng, J. Groenesteijn, D. Alveringh, R. J. Wiegerink, and J. C. Lötters, “Design, fabrication, and characterization of a micro Coriolis mass flow sensor driven by PZT thin film actuators,” Journal of Microelectromechanical Systems, vol. 30, no. 6, pp. 885-894, 2021.

[13] C. Huber, “MEMS-based micro-Coriolis density and flow measurement technology,” in Proc. AMA Conferences, pp. 157-162, 2015.

[14] N. Anderson, Bond Strength Characterization of SU-8 to SU-8 for Fabricating Microchannels of an Electrokinetic Microfluidic Pump, 2012.

[15] Istituto Nazionale di Ricerca Metrologica (INRiM), Procedura di lavoro sicuro: Gestione Laboratorio PiQuET – Regole di vestizione e buone norme di comportamento in Clean Room, Istruzione Operativa IO SPP PLS N00 01, Ed. 0, Rev. 0, 2021.

[16] Kayaku Advanced Materials, Inc., OmniCoat Safety Data Sheet, Version 8, Sept. 9, 2019.

[17] Istituto Nazionale di Ricerca Metrologica (INRiM), Procedura di lavoro sicuro: Gestione Laboratorio PiQuET – Manipolazione in sicurezza di prodotti chimici, utilizzo in sicurezza di cappe chimiche e degli armadi, Codice IO SPP PLS N05ab.

[18] Carlo Erba Reagents S.r.l., Safety Data Sheet: Acetone, SDS CH0014, Version 37, 2020.

[19] Carlo Erba Reagents S.r.l., Safety Data Sheet: Isopropyl Alcohol, SDS CH0040, Version 36, 2024.

[20] SPS-Europe B.V., Polos SPIN150i/200i Infinite Spin Processing System – Operating Instruction, Software Rev. 1.11, 2026.

[21] MicroChemicals GmbH, Safety Data Sheet: PGMEA, Revision 1.01, Jan. 25, 2024.

[22] KLA Corporation, P-17/P-7 Profiler User Manual, Version 9.0, P/N 9030487-000, Rev. AA, 2022.

[23] Olympus Corporation, DSX1000 Digital Microscope: Hardware Manual, 2019.

[24] Fluigent, LineUp Series User Manual, Version 3, 2020.

[25] Stratasys Ltd., Stratasys J3 Series 3D Printing System – User Guide, DOC-19001 Rev. I, 2023.

[26] Polytec GmbH, MSA-060 Micro System Analyzer: Technical Datasheet, 2024.

[27] "Polytec GmbH. (2024). VibroFlex Connect front-end and VibroFlex Compact [Technical datasheet]. Polytec GmbH.".

[28] N. LaBianca, J. Gelorme, K. Lee, E. Cooper, E. O'Sullivan, and J. Shaw, "High aspect ratio optical resist chemistry for MEMS application," Electrochemical Society Proceedings, vol. 95, no. 18, pp. 386-396, 1993.

[29] O. P. Parida and N. Bhat, "Characterization of optical properties of SU-8 and fabrication of optical components," in Proc. International Conference on Optics and Photonics (ICOP), 2009.

[30] L. H. Tam and D. Lau, "Characterizing mechanical properties of polymeric material: A bottom-up approach," in Handbook of Mechanics of Materials. Singapore: Springer, 2018, pp. 57-93.

[31] R. Feng and R. J. Farris, "Influence of processing conditions on the thermal and mechanical properties of SU-8 negative photoresist coatings," Journal of Micromechanics and Microengineering, vol. 13, no. 1, pp. 80-88, 2003.

[32] T. Namazu, S. Inoue, K. Takio, T. Fujita, K. Maenaka, and K. Koterazawa, "Visco-elastic properties of micron-thick SU-8 polymers measured by two different types of uniaxial tensile tests," in Proc. IEEE MEMS, 2004, pp. 147-150.

[33] Kayaku Advanced Materials, Inc., OmniCoat Adhesion Promoter/Release Layer Technical Data Sheet, 2020.

[34] A. Campo and C. Greiner, "SU-8 photoresist for microsystems," Journal of Micromechanics and Microengineering, vol. 17, no. 6, pp. R81-R121, 2007.

[35] M. R. Haq and H. Schift, “Vertical sidewalls in thick epoxy resists: A challenge for laser-based direct-write lithography,” Micro and Nano Engineering, vol. 19, Art. no. 100210, 2023.

[36] MicroChem Corp., SU-8 2000 Permanent Epoxy Negative Photoresist: Processing Guidelines for SU-8 2100 and SU-8 2150, Technical Data Sheet.

[37] P. Wattanachai and C. Antonio, “Comparison of conventional and variable frequency microwave curing of SU-8 photoresist: Effects on the dielectric, thermal, and morphological properties,” Engineering Journal, vol. 18, no. 4, pp. 91-100, 2014.